# Numerical Simulation of Mountain Waves over the Southern Andes. Part II: Momentum Fluxes and Wave–Mean-Flow Interactions

DAVID C. FRITTS,[a,b] THOMAS S. LUND,[a] KAM WAN,[a] AND HAN-LI LIU[c]

[a] *GATS, Boulder, Colorado*
[b] *Embry–Riddle Aeronautical University, Daytona Beach, Florida*
[c] *HAO, NCAR, Boulder, Colorado*

(Manuscript received 6 July 2020, in final form 24 November 2020)

ABSTRACT: A companion paper by Lund et al. employed a compressible model to describe the evolution of mountain waves arising due to increasing flow with time over the southern Andes, their breaking, secondary gravity waves and acoustic waves arising from these dynamics, and their local responses. This paper describes the mountain wave, secondary gravity wave, and acoustic wave vertical fluxes of horizontal momentum, and the local and large-scale three-dimensional responses to gravity breaking and wave–mean-flow interactions accompanying this event. Mountain wave and secondary gravity wave momentum fluxes and deposition vary strongly in space and time due to variable large-scale winds and spatially localized mountain wave and secondary gravity wave responses. Mountain wave instabilities accompanying breaking induce strong, local, largely zonal forcing. Secondary gravity waves arising from mountain wave breaking also interact strongly with large-scale winds at altitudes above ~80 km. Together, these mountain wave and secondary gravity wave interactions reveal systematic gravity wave–mean-flow interactions having implications for both mean and tidal forcing and feedbacks. Acoustic waves likewise achieve large momentum fluxes, but typically imply significant responses only at much higher altitudes.

KEYWORDS: Atmosphere; Gravity waves; Mountain waves; Nonlinear models; Mountain meteorology

## 1. Introduction

Mountain wave (MW) studies have a history spanning over 100 years (Smith 2019). A survey of the earliest studies was presented in the review of the Sierra Wave Project occurring in the 1950s by Grubišić and Lewis (2004). Increasingly quantitative airborne and ground-based studies over the Rockies in the 1970s addressed conditions contributing to strong MW breaking, momentum fluxes (hereafter MFs), and turbulence in the upper troposphere and lower stratosphere (see Lilly and Kennedy 1973; Lilly 1978) and motivated multiple modeling and theoretical efforts thereafter (Klemp and Lilly 1978; Durran and Klemp 1987; Durran 1990, 1995; Smith 1979).

Other observations provided evidence of the importance of MWs relative to gravity waves (GWs) arising from other sources in the troposphere and lower stratosphere. Measurements during the Global Atmospheric Sampling Program (GASP) from 1975 to 1979 enabled assessments of contributions by various GW sources to flight-level variances. Various GASP studies revealed variance enhancements up to ~6 times larger over mountains than over plains and oceans and up to ~10 times larger over terrain having the highest roughness (Nastrom et al. 1987; Jasperson et al. 1990). Stratification of these data by GW source revealed that mean variances over orography 1) exceeded those over convection, frontal systems, and jet streams, 2) were ~40%–150% larger than the second largest source, jet streams, for velocities, and 3) that MW zonal MFs were generally negative and occurred primarily at horizontal wavelengths $\lambda_h \sim$ 25–60 km (Nastrom and Fritts 1992; Fritts and Nastrom 1992), confirming the likely importance of MWs in the atmosphere.

The 1999 Mesoscale Alpine Programme (MAP), the 2006 Terrain-Induced Rotor Experiment (T-REX), and other programs employed increasingly capable airborne and ground-based measurements in a variety of regions. These observations and parallel modeling significantly expanded our understanding of MW sensitivity to source characteristics, surface influences, and propagation conditions extending into the lower stratosphere (e.g., Bougeault et al. 2001; Doyle et al. 2005; Jiang and Doyle 2004; Jiang et al. 2006; Smith et al. 2007, 2008; Grubišić et al. 2008). None of these programs included measurements above aircraft altitudes, however, so were unable to address MW responses above the lower stratosphere.

Initial modeling extending into the mesosphere suggested MW penetration, breaking, and significant drag (Bacmeister 1993; Bacmeister and Schoeberl 1989; Satomura and Sato 1999; Schoeberl 1985). Global satellite measurements expanded sensitivity to GW responses in the stratosphere to sources at lower altitudes. Analyses of these data provided evidence of MWs in the middle and upper stratosphere having distinct "hotspots" over high orography at middle to high latitudes in winter (Eckermann and Preusse 1999; Jiang et al. 2002; Wu and Eckermann 2008; Alexander and Grimsdell 2013; Hendricks et al. 2014; Hoffmann et al. 2013). Nadir, limb, and sublimb

Denotes content that is immediately available upon publication as open access.

Supplemental information related to this paper is available at the Journals Online website: https://doi.org/10.1175/JAS-D-20-0207.s1.

*Corresponding author*: Thomas Lund, lund@gats-inc.com

DOI: 10.1175/JAS-D-20-0207.1

observations provided insights into spatial distributions in the stratosphere, but in all cases underestimated MW amplitudes and failed to capture smaller spatial scales due to line-of-sight integration across GW structures.

MWs in the mesosphere and lower thermosphere (MLT) over the southern Andes first reported by Smith et al. (2009) exhibited stationary phases aligned approximately north–south, horizontal wavelengths $\lambda_h \sim$ 35–40 km, and were seen in three airglow emissions from ~87 to 96 km. Observations by Smith et al. (2013) over New Zealand revealed apparent MW breaking at ~80–100 km and larger-scale secondary GWs (SGWs) at ~250 km, similar to SGWs generated by stratospheric GW breaking (Sato et al. 2009).

More extensive contributions to understanding MW propagation and influences in the stratosphere and MLT accompanied the Deep Propagating Gravity Wave (DEEPWAVE) program conducted over New Zealand in 2014 (Fritts et al. 2016). DEEPWAVE was motivated by the studies noted above and the limited evidence of MWs able to achieve MLT altitudes in winter. DEEPWAVE comprised 26 research flights performing lidar profiling from ~25 to 105 km, OH airglow temperature imaging at ~87 km along and across the flight tracks, and ground-based imaging and lidar profiling east of the Southern Alps on the New Zealand South Island. DEEPWAVE results relevant to the study described here include the following:

1) strong forcing can yield large MWs and MW breaking at lower altitudes and in the MLT (Kaifler et al. 2015; Bramberger et al. 2017),
2) large-amplitude MWs in the MLT can result from weak (strong) flow over significant (lower) orography (Eckermann et al. 2016, hereafter E16; Pautet et al. 2016, hereafter P16; Bossert et al. 2015, 2018, hereafter B15, B18; Fritts et al. 2018, 2019, hereafter F18, F19; Taylor et al. 2019, hereafter T19),
3) GW instabilities are largely consistent with model predictions of instability forms and MW amplitude decreases (P16; F18, F19; T19),
4) MW MFs as large as $\langle u_h' w' \rangle \sim 600$–$800\,\mathrm{m^2\,s^{-2}}$ (for horizontal and vertical perturbation velocities, $\langle u_h' \rangle$ and $w'$, and brackets denoting a horizontal average) accompany MW $\lambda_h \sim$ 100 km or smaller in the MLT (P16; F18, F19; T19), and
5) SGW generation accompanies MW breaking dynamics (B15).

Ground-based observations on Tierra del Fuego (53.8°S, 67.7°W) during austral winter 2018 provided MF assessments SE of the major southern Andes terrain. Rayleigh lidar observations aided by ECMWF modeling yielded peak $\rho_0 \langle u_h' w' \rangle \sim 30$–$200\,\mathrm{mPa}$ at 40–50 km (Kaifler et al. 2020). A related study using airglow imaging and radar winds at ~80–90 km at the same site yielded MFs often $\sim 100\,\mathrm{m^2\,s^{-2}}$ or larger and exhibiting strong semidiurnal tide modulation (Pautet et al. 2021).

Model results described by Lund et al. (2020, hereafter L20) include many aspects that are consistent with DEEPWAVE observations described above, despite having very different orography. These include the following:

1) initial breaking in the MLT where the zonal wind $U$ becomes small and the MWs approach a critical level,
2) strong MW breaking in the MLT at $\lambda_h \sim$ 40–70 km east of the southern Andes and extending ~200–300 km downstream, and also at larger $\lambda_h$ upstream at higher altitudes and later times,
3) SGW radiation to higher altitudes from MW breaking below, and
4) MLT MW breaking extending for ~1000 km along the southern Andes at later times.

This paper employs further results of the MW simulation described by L20 expanding on those summarized above. These include assessments of 1) MW, SGW, and acoustic wave (AW) MFs at lower and higher altitudes and extended along the southern Andes, 2) local $U$ departures from initial fields driven by MF divergence, 3) nonlocal responses to local mean forcing, and 4) correlations of MW and SGW MFs due to filtering by large-scale shears.

Our paper is organized as follows. Section 2 summarizes the model configuration and analysis methods. Mean-flow and MF evolutions are presented and compared in section 3. Section 4 describes mean forcing, flow evolution, and correlations with mean winds and shears. Sections 5 and 6 provide a discussion of these results in relation to previous studies and our conclusions.

## 2. Model capabilities and configuration and data analysis methods

### a. *Model capabilities and configuration*

The Complex Geometry Compressible Atmospheric Model (CGCAM) is a finite-volume code that solves the compressible Navier–Stokes equations (see L20). It employs exponential mesh stretching enabling very high resolution where required to resolve initial instabilities due to MW and SGW breaking. The computational domain extended 2500 km in longitude, 2000 km in latitude, and 200 km in altitude and was centered at 48.2°S between the two major southern Andes massifs ~120 km north and south (~47.1° and 49.3°S) denoted N and S peak (NP and SP). Isotropic 500-m resolution was employed from roughly −50 to 250 km in $x$ and −400 to 350 km in $y$ relative to the domain center, and from $z$ = 0–200 km (Fig. 1, left).

Inflow–outflow boundary conditions were employed, and damping layers were specified at the lateral and upper boundaries in order to absorb outgoing GWs and AWs. Impacts of smaller scales following transition to instabilities was defined by the dynamic subgrid-scale (SGS) scheme of Germano et al. (1991). Resolution of the initial instabilities ensures that they have realistic impacts on MW and SGW amplitudes and evolutions.

Initial conditions include horizontally uniform wind and temperature fields specified by a free-running WACCM at 50°S (right panels in Fig. 1). These exhibit significant cross-mountain flow up to $30\,\mathrm{m\,s^{-1}}$ over the major southern Andes peaks, and generally increasing zonal winds up to a strong maximum of $\sim 190\,\mathrm{m\,s^{-1}}$ at ~47 km, decreasing to a minimum of $\sim 10\,\mathrm{m\,s^{-1}}$ at ~87 km, increasing to $\sim 170\,\mathrm{m\,s^{-1}}$ at ~100 km, and decreasing to an initial MW critical level at

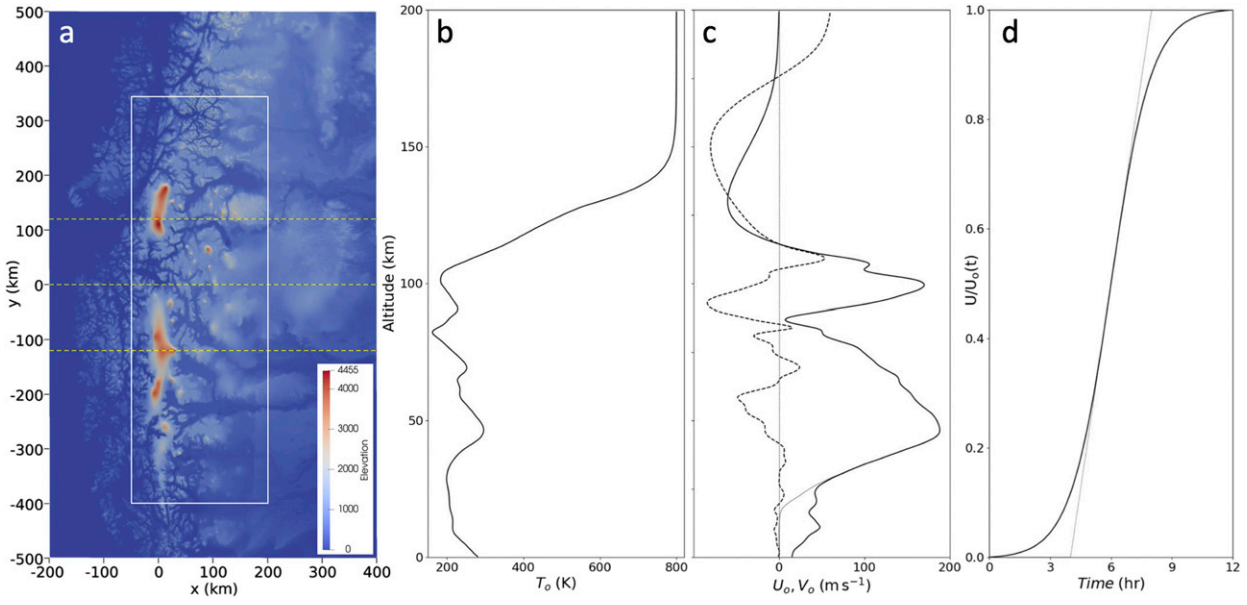


FIG. 1. (a) Southern Andes terrain elevations and WACCM winter profiles of (b) $T_0$, and (c) $U_0$ and $V_0$ (solid and dashed, respectively) up to ~105 km at 50°S and 73°W, with analytic extensions to higher altitudes. (d) The prescribed temporal variation of the lower-level $U_0$ deficit below 20 km [thin dashed line at bottom in (c)] is shown. The CGCAM region having 500-m isotropic resolution extending 250 km is longitude and 750 km in latitude is shown with the white rectangle in (a).

~115 km. Meridional winds were in quadrature with zonal winds above ~70 km, as expected for the semidiurnal tide. WACCM temperatures also exhibited significant variability, and implied strong variations of mean static stability $N_0^2$ leading to regions of evanescence for MWs having smaller $\lambda_h$. WACCM wind and temperature profiles were artificially extended to higher altitudes by approximating tidal winds and assuming a solar-mean thermospheric state. A free-slip lower boundary was assumed, and MWs were excited by imposing a gradual ramp of the winds from the surface to 25 km over 12 h to approximate slowly varying mesoscale conditions (Fig. 1, right).

Initial and evolving zonally averaged zonal and meridional mean wind are denoted ($U_0$, $V_0$) and ($U$, $V$), with local zonal departures from initial conditions $\Delta U = U - U_0$. Perturbations and the total evolving zonal fields are denoted ($u'$, $v'$, $w'$) and $u = U + u'$. Perturbation fields have component wavelengths ($\lambda_x, \lambda_y, \lambda_z$) and wavenumbers ($k = 2\pi/\lambda_x, l = 2\pi/\lambda_y, m = 2\pi/\lambda_z$) with $k_h^2 = k^2 + l^2$ and $\lambda_h = 2\pi/k_h$. Other quantities include phase speed $c$, intrinsic phase speed $c_i = c - U_h$ for $U_h$ in the plane of GW propagation, intrinsic frequency $\omega_i = k_h c_i$, and buoyancy frequency and period, $N_0$ and $T_b = 2\pi/N_0$.

### b. Data analysis methods

While the primary solution variables are displayed without spatial averaging, such averaging must be applied for the MFs and for the mean-flow deviations. Given our exploration of MFs for MW $\lambda_x \sim$ 40–70 km east of the southern Andes and at higher altitudes upstream, and our desire to estimate local MFs and responses, we employ a raised cosine window with a full-width/half-maximum (FWHM) of 100 km or larger along $x$ (depending on altitude, variable, and relevant GW scale) to assess local $U$, $\Delta U$, and MFs (see text for details in each case).

## 3. MW, SGW, and AW evolutions and momentum fluxes

We quantify in this section MW and SGW vertical fluxes of zonal momentum, $\langle u'w' \rangle$, and their sources and roles in driving departures from the initial mean fields where these fluxes are divergent. We first describe the MW, SGW, and AW evolutions revealed in $u = U + u'$ $x$–$z$ cross sections over SP and NP, and in $y$–$z$ cross sections at several locations across the southern Andes terrain. These are shown at left in Figs. 2–4, respectively, and corresponding $\langle u'w' \rangle$ fields are shown at right. $\langle v'w' \rangle$ magnitudes (not shown) are generally much smaller and arise initially through three-dimensional (3D) MW self-acceleration (SA) dynamics (Fritts et al. 2020, hereafter F20) exhibiting local meridional negative maxima of $dU/dt$ that bow the local MW phase westward and imply increasing (decreasing) $\langle v'w' \rangle$ to the north (south). MF units are m$^2$ s$^{-2}$, given the units employed for MLT observational studies of these dynamics in order to compare with MLT observations. We also discuss these MFs in pascals in a comparison to stratospheric observations in section 5.

### a. MW evolution

The MW field evolution over SP is shown with $u(x, z)$ cross sections from 7.5 to 11 h at left in Fig. 2. Weak initial MW amplitudes over and east of SP enable linear propagation to $z \sim$ 100 km by ~7 h. Increasing $u'$ due to increasing cross-mountain flow leads to initial MW breaking prior to ~7.5 h above $z \sim$ 70 km approaching the minimum initial $U_0$ ~ 10 m s$^{-1}$ at ~87 km, with smaller amplitudes approaching

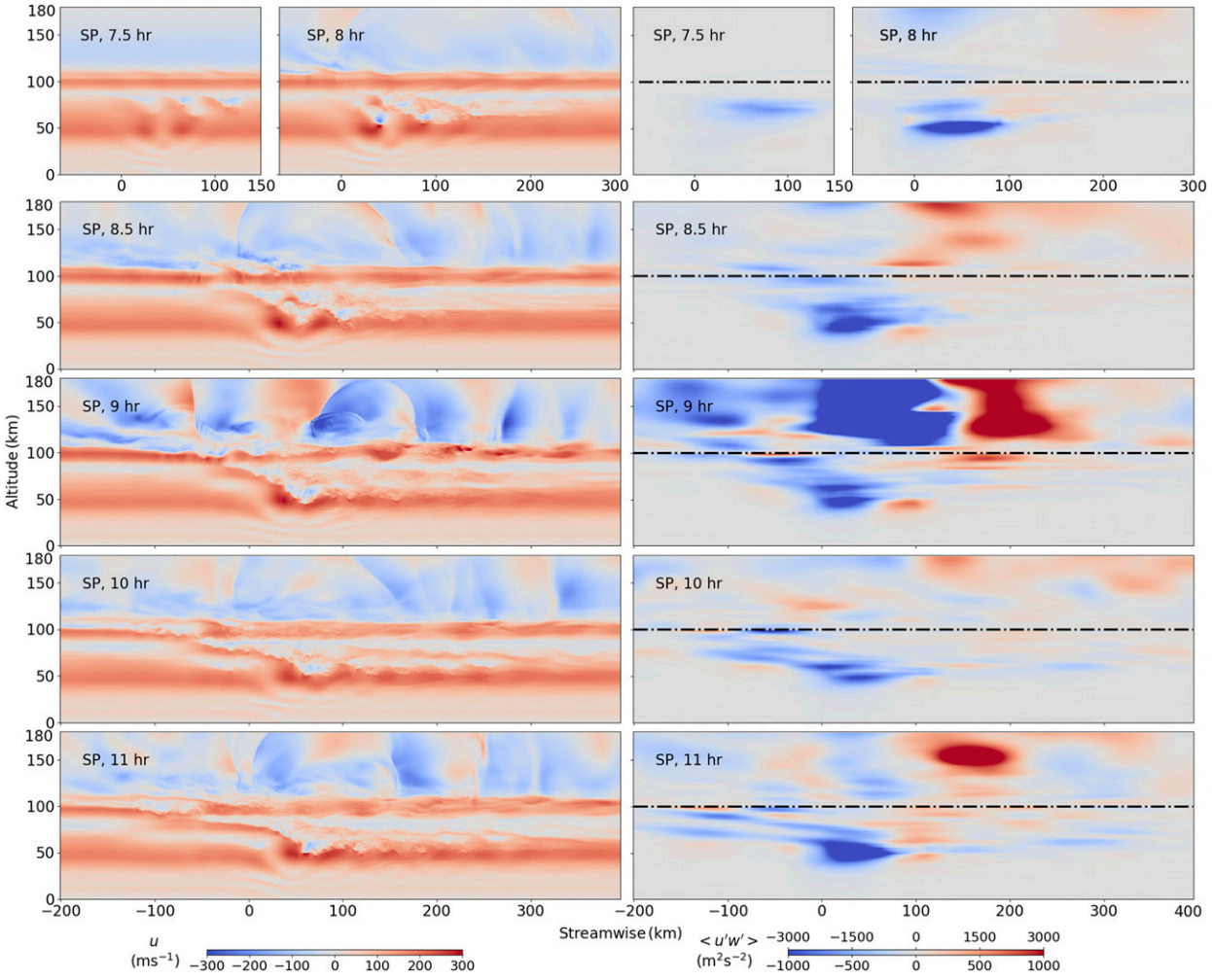


FIG. 2. (left) $u(x, z)$ and (right) $\langle u'w' \rangle$ $(x, z)$ over SP from $z$ = 0–180 km and 7.5–11 h. The dashed black lines at 100 km in the right panels show the transition from the lower to the upper color scale for $\langle u'w' \rangle$ shown at bottom right.

the MW critical level at $z$ = 115 km (Fig. 2 at left, top left). The $u(x, z)$ cross sections from 8 to 9 h show MW breaking to intensify and descend to below the peak $U$ at $z \sim 47$ km, extend downstream to $x \sim 170$ km below $z \sim 85$ km, and extend upstream >100 km west of SP at $z \sim 100$–115 km. Thereafter, breaking extends to over 250 km downstream, more weakly and confined to $z \sim 60$–70 km over SP at $z \sim 70$–80 km, and more strongly upstream at ~100–110 km, in each case confined by decreasing $U$ with altitude above (see online supplementary movies).

The evolution in the $x$–$z$ plane over NP (Fig. 3, left) differs in significant ways from that over SP. The more localized NP E–W terrain causes a more extended and energetic breaking MW train downstream of the terrain throughout the evolution. However, breaking east of NP also descends only to $z \sim 52$ km, ~7 km higher than east of SP (also see Figs. 4 and 5 below). Breaking is also less intense over NP, based on $|u'|$ maxima in breaking regions and the implied larger $\lambda_z > 2\pi U/N$ (due to nonhydrostatic MWs in large $U$) at breaking altitudes over SP.

The different responses over SP and NP suggest significant variations along the Andes in responses to varying terrain heights and scales. To investigate the implications for the MW and SGW fields and MFs, $u(y, z)$ cross sections and zonal MFs averaged along $x$ as in Figs. 2 and 3 are shown from 8 to 10 h at $x$ = 0, 50, and 100 km at left and right in Fig. 4. To aid interpretation of these fields, we note that blue colors at left denote westward $u = U + u'$, hence implied overturning and breaking at altitudes below the MW critical level at $z$ = 115 km.

MW responses at 8 h are very weak over the southern Andes at $x$ = 0, but exhibit initial overturning at $z \sim 70$–90 km over SP and increasing amplitudes approaching the MW critical level between SP and NP. Initial responses noted above are much more pronounced at $x$ = 50 and 100 km at 8 h east of SP, but not seen east of NP because the smaller MW $\lambda_x \sim 50$ km at this location yields warm phases of the MW response at these locations.

The $u(y, z)$ cross sections at left in Fig. 4 also provide important insights into the larger-scale responses to the variable

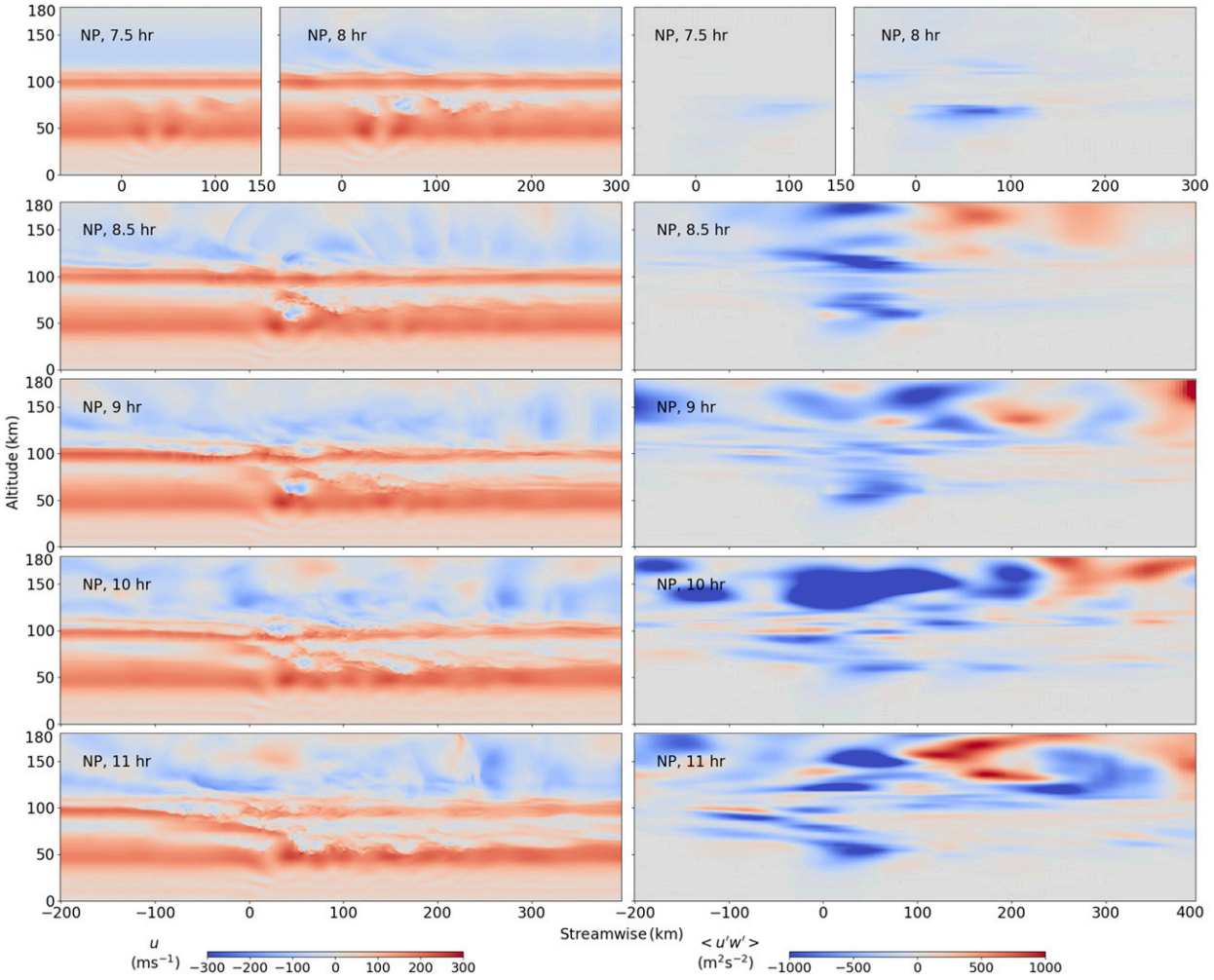


FIG. 3. As in Fig. 2, but over NP. The same $\langle u'w' \rangle$ color scale is used for all $z$ in this case.

MW and MF influences. Seen at $x = 50$ km at 8 h, and with larger amplitudes at 8.5 h, are regions of increased $U$ along $y$ between and below the breaking regions east of SP and NP. Similar, but weaker, responses are also discernable at $x = 0$ and with greater variability in $y$ at $x = 100$ km extending to later times.

Comparing the responses at $x = 0$, 50, and 100 km, we see that the major MW breaking remains east of the southern Andes accompanying the initial MW response. The deepest descents of MW breaking persist east of SP and NP, with that over NP remaining weaker and confined to higher altitudes. See the light blue regions at 8.5 and 9 h and $x = 50$ km east of SP and NP above $z \sim 45$ and 55 km, respectively, having meridional widths of ~50–100 km. Also note the regions of significantly enhanced (positive) $U$ between, and north and south of, both MW breaking responses, especially at $x = 50$ km, with weaker and more variable responses at $x = 100$ km. Regions of enhanced $U$ exhibit no instabilities and are instead indications of compensating stronger eastward winds where MW breaking yields MF gradients implying strong flow decelerations.

The subsequent evolution of this flow reveals that MW breaking extends further N and S along the southern Andes at $x = 50$ and 100 km by 10 h, and that the response at $x = 50$ km becomes less variable along $y$ with time. Additionally, responses at $x = 100$ km deviate significantly from those at $x = 50$ km accompanying attainment of the strongest responses at ~9 h, revealing instability occurrence and $U$ variability that are more nearly anticorrelated with those at $x = 50$ km, $|y| < 250$ km, and 9 and 10 h. See, as examples, the deeper MW breaking descents at $y \sim -200$, 50, and 200 km at $x = 100$ km and 10 h, where the corresponding descents at $x = 50$ km are smaller than elsewhere.

Another perspective on these dynamics is provided by $u'(x, y)$ cross sections at 50 and 70 km altitudes at 8, 9, and 10 h and at 100 km at 9 and 10 h on the left half of Fig. 5. These altitudes correspond to the lower and higher regions of major MW breaking in the mesosphere and at the altitude of maximum $U$ below the MW critical level in the thermosphere. The fields at 50 and 70 km show that the zonal responses expand rapidly downstream and along the southern Andes from 8 to 9 h, as inferred from Figs. 2–4 at specific $x$ and $y$. They also confirm

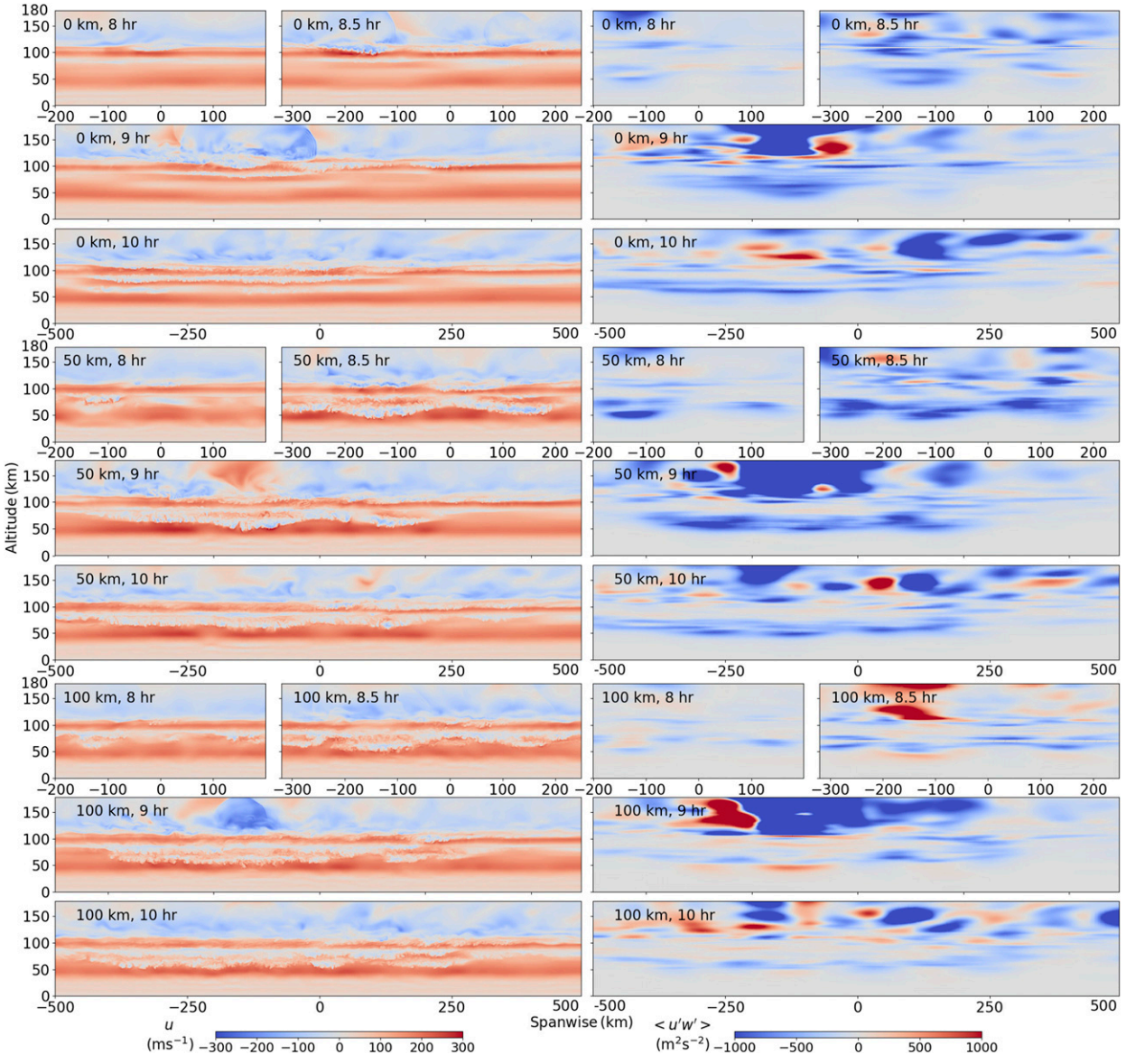


FIG. 4. As in Figs. 2 and 3, but for $u(y, z)$ and $\langle u'w' \rangle (y, z)$ from 8 to 10 h at $x =$ (top) 0, (middle) 50, and (bottom) 100 km.

that MW breaking quickly extends to lower altitudes over SP, but remains above 50 km over NP as these regions approach their peak responses. Important features include 1) the well-delineated responses east of SP and NP at the earlier times, 2) clear decelerations of $U$ at 70 km initially east of SP and NP, but increasingly to the south at 9 and 10 h (blue regions with MW phases bowed westward at the center), 3) expanded decelerations of $U$ at 100 km exhibiting large bow-wave responses over ~800 km N–S at 9 and 10 h, and 4) significant upstream penetration of $U$ decelerations extending west at these times.

Not shown, but implied by these responses, are related $v'$, $\langle v'w' \rangle$, and $V$ where nonzero $dU/dy$ rotates MW orientations and induces horizontal convergence and divergence in the local mean horizontal flow. Because the MW orientations remain largely along $x$, however, the induced responses are smaller, but they do contribute to spanwise and vertical variations in observed $U$.

### b. *MW instability dynamics*

We briefly address the instability dynamics accounting for MW breaking to provide confidence in their implications for the MW evolution and the resulting SGW and AW generation, pseudomomentum deposition, and mean-flow responses discussed below. These are illustrated with limited $x$–$z$ cross sections of spanwise vorticity over SP, $\zeta_y$, and $x$–$y$ cross sections of $w$ at 70 and 100 km altitudes in Fig. 6. These fields reveal that initial instabilities comprise vortex rings, as seen to accompany MW and more general GW breaking in idealized modeling and OH airglow and polar mesospheric cloud

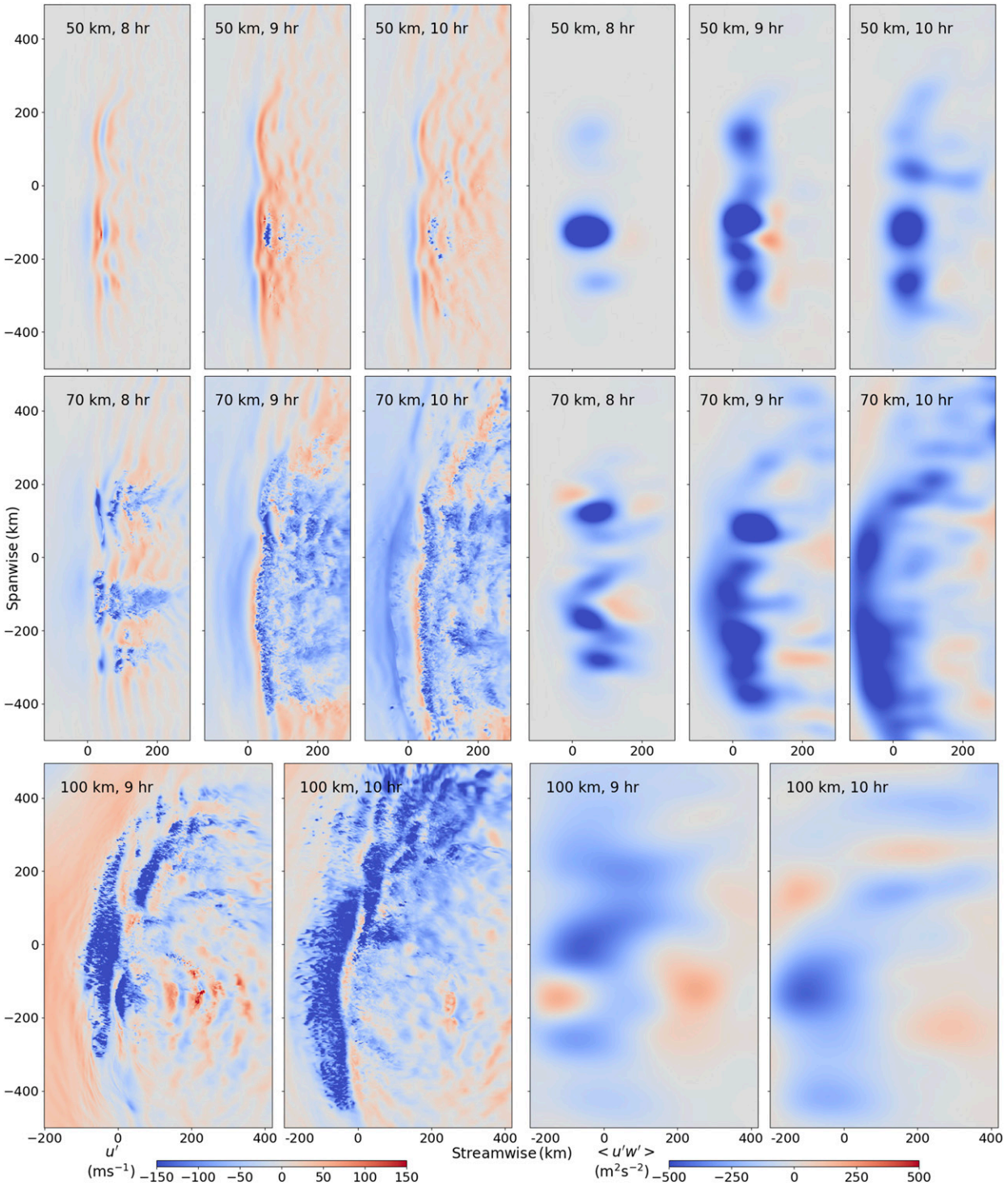


FIG. 5. As in Fig. 4, but for $u'(x, y)$ and $\langle u'w' \rangle (x, y)$ at (top),(middle) $z = 50$ and 70 km and 8, 9, and 10 h and at (bottom) $z = 100$ km and 9 and 10 h. $\langle u'w' \rangle$ in the right panels is averaged with a FWHM = 100 (50) km along $x$ ($y$) at 50 and 70 km and a FWHM = 200 (100) km at 100 km.

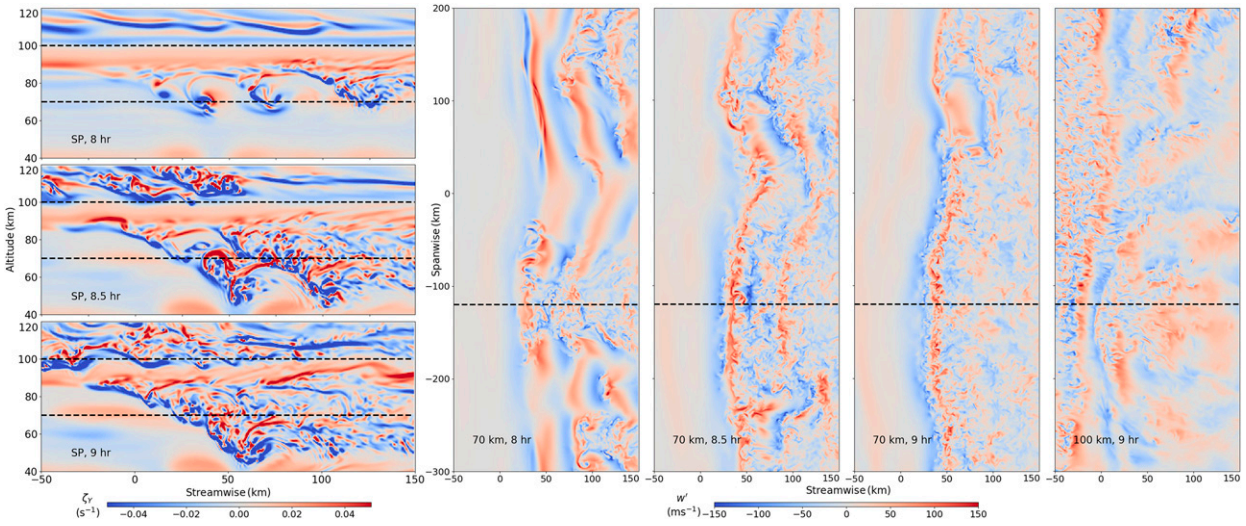


FIG. 6. (left, top to bottom) $\zeta_y(x, z)$ over SP at 8, 8.5, and 9 h for $x$ from −50 to 150 km and $z$ = 40–120 km and (right, left to right) $w(x, y)$ at $z$ = 70 km and 8, 8.5, and 9 h and at $z$ = 100 km at 9 h.

imaging (Fritts et al. 2009a,b, 2017, hereafter F09a,b; F19; Hecht et al. 2018). Vertical cross sections of vortex rings are revealed by the tilted positive and negative (upper left and lower right) $\zeta_y$ maxima seen most clearly at the leading edge of each descending MW phase at 8 h (Fig. 6, top left). Evidence of vortex rings are also seen in the $x$–$y$ cross sections of $w$, where descending motions (blue) occur within rings of ascending motions (red) near the transitions from descending to ascending MW phases. In both $x$–$z$ and $x$–$y$ cross sections, vortex ring scales range from ~5 to 10 km or larger, and are consistent with expectations for ring diameters to be ~0.3–0.4$\lambda_z$ for idealized nonhydrostatic GWs (F09b; F17).

### c. SGW and AW evolutions

SGWs at larger scales arise due to localized body forces accompanying transient GW MF gradients, whether they are large or small. As described by Dong et al. (2020, hereafter D20) and F20, SGW generation is strongest where GW phase steepening leads to stalling of the GW vertical propagation and associated SA dynamics. Importantly, however, not all induced mean flows lead to GW stalling. SGW generation also accompanies local GW instability dynamics, whether or not the initial GW undergoes SA dynamics, with spatial scales dictated by these local dynamics.

AWs arise primarily due to GW breaking yielding strong, transient compressible dynamics. Neither SGWs nor AWs have large amplitudes at their source altitudes, however, but require propagation over multiple scale heights, $H$, above the MW breaking regions to become visible in the presence of large-amplitude MWs. As a result, both SGWs and AWs are most apparent above the MW critical level at $z$ = 115 km. AWs are easier to identify where large amplitudes result in roughly spherical shapes having sharp phase transitions. SGW phase variations and $\lambda_h$ can resemble MWs, but can be discriminated by their large nonzero phase speeds and often nonzonal propagation directions (see online supplementary movies).

Specific SGW responses seen in Figs. 2–4 and 7, and the accompanying movies include

1) largely upstream and downstream SGW propagation at $z >$ 115 km arising quickly after MW breaking with $\lambda_x \sim$ 50–200 km, $c \sim$ 100–200 m s$^{-1}$, and $\lambda_x$, $\lambda_z$, and $c$ increasing with altitude,
2) weaker SGWs at $z >$ 115 km at larger radii (Fig. 4, left, at 9 and 10 h), and
3) eastward-propagating ducted SGWs at $z \sim$ 87–105 km, $\lambda_x \sim$ 65 km, and $c \sim$ 230 m s$^{-1}$ by ~8.5 h.

AW responses seen in Figs. 2–4 and 7 and the accompanying movies include

1) emergence from the regions of strongest initial MW breaking beginning at ~7.5 h,
2) large amplitude increases, especially over SP where MW breaking is lower and stronger,
3) roughly spherical phase fronts and sharp phase transitions above $z \sim$ 105 km, and
4) propagation upward and outward from regions of strong MW breaking yielding large amplitudes and dramatic phase variations to $z$ = 180 km and ~300 km horizontally.

Following initial MW breaking, SGWs and AWs make major contributions to flow variability via transient ($u'$, $v'$, $w'$, $T'$) above ~87 km. However, their larger scales and higher frequencies allow them to avoid significant dissipation, hence they contribute little to mean field evolutions.

### d. MW, SGW, and AW MF evolutions

We now examine the zonal MFs accompanying the MW evolution. The $x$–$z$ cross sections of $\langle u'w' \rangle$ averaged along $x$ ($y$) with FWHM of 100, 100, and 200 (50, 50, and 100) km at $z$ = 50, 70, and 100 km are shown over SP and NP at right in Figs. 2 and

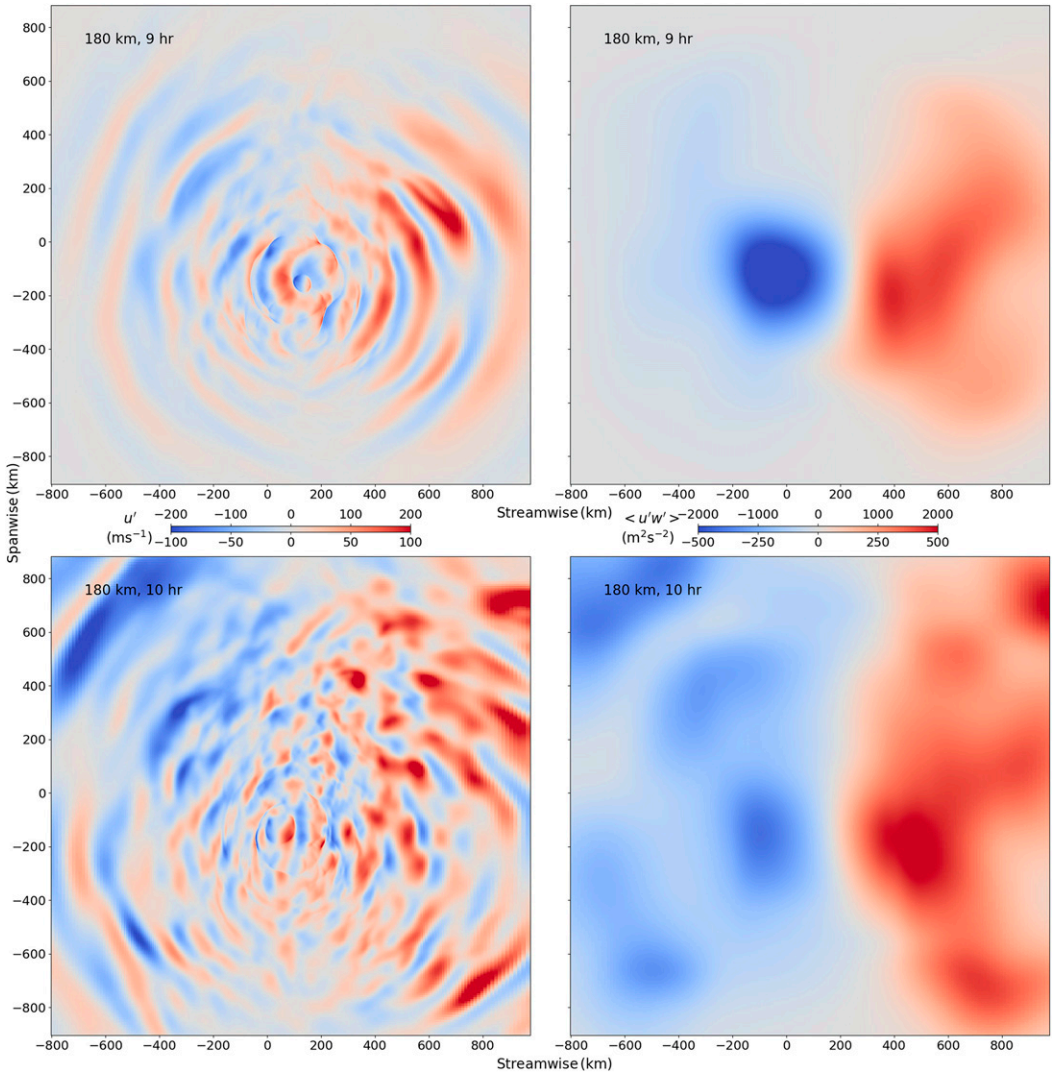


FIG. 7. As in Fig. 5, but at $z = 180$ km and (top) 9 and (bottom) 10 h. $\langle u'w' \rangle$ in the right panels are averaged with a FWHM = 300 km in $x$ and $y$.

3. Note the different color scales for $\langle u'w' \rangle$ above and below 100 km shown at right in Fig. 2 to enable better estimates of the sporadic, large SGW and AW MFs at higher altitudes. The $y$–$z$ cross sections of $\langle u'w' \rangle$ at $x = 0$, 50, and 100 km averaged as above are shown at right in Fig. 4. The $x$–$y$ cross sections at $z =$ 50, 70, and 100 km are shown at right in Fig. 5. Figure 7 at right shows $x$–$y$ cross sections of $\langle u'w' \rangle$ at 180 km averaged with a 300-km FWHM in $x$ and $y$, given the larger SGW $\lambda_h$ and their variable orientations.

MW MFs at the onset of breaking east of SP at $x \sim 80$ km, $z \sim 70$ km, and ~7.5 h are large (maxima $\sim -600$ m$^2$ s$^{-2}$). Increasing MW amplitudes in larger $U$ yield MFs $\sim -500$ to $-1200$ m$^2$ s$^{-2}$ from $z \sim 45$–60 km and retain the higher initial maximum at 8 h. Thereafter, MF responses in the region of primary MW breaking extend from $x \sim 0$–100 km and $z \sim 40$–80 km, exhibit extended regions having MFs $\sim -1000$ m$^2$ s$^{-2}$ or larger, and have variable structure in altitude and time due to nonstationary MW breaking. MW MFs at these altitudes are more variable and weaker further E. Thin regions with negative MFs accompany MWs extending further downstream with time (Fig. 2), especially at $z \sim 50$–80 km and $x \sim 100$–200 km at 9 h and sporadically at $z \sim 50$–70 km thereafter.

Below $z \sim 115$ km over and upstream of SP from 8.5 to 11 h are regions of negative and positive MF. Negative MFs accompany upward propagation of higher $\omega_i$ MWs over and east of SP at earlier times and of larger-scale and lower $\omega_i$ MWs extending increasingly upstream with time (Fig. 2, left). Positive MF maxima along the larger-scale MW phase upward toward W arise from inadequate horizontal averaging over these larger-scale MWs. MW MFs over NP below $z = 115$ km are similar to those over SP, but differ in the details because of the weaker and more extended NP downstream response. Specific differences include the following:

1) peak MW MFs east of NP in the stratosphere arise more slowly, descend only to ~52 km, ~10 km higher than east of SP, and have ~30%–50% smaller maxima at these times,
2) unlike SP, which has small MFs above ~100 km, NP MWs have MFs ~−500 to −800 $m^2 s^{-2}$ that arise due to upward propagation of the lee MWs extending further E, and
3) upstream MFs due to larger $\lambda_x$ MWs emanating from the region of major MW breaking arise somewhat later over NP due to the delayed and less intense breaking east of NP.

MFs at higher altitudes emerge quickly after the earliest MW breaking east of SP at ~50–80 km (Fig. 2, right, at 8 h above 150 km). Figure 2 at left and SM1.mp4 show these to accompany initial AWs, because initial SGWs are propagating largely westward and confined to $z < 150$ km at 8 h. Both AW and SGW MFs increase dramatically up to ~9 h, exhibit largely positive (negative) MFs E (W) of primary MW breaking below, and achieve large magnitudes more intermittently thereafter. Of these, AWs account for the major MFs above ~110 km, exhibiting transient, but nearly continuous positive (negative) magnitudes of ~1500 (1000) $m^2 s^{-2}$ or larger at 8.5 h and ~3000 (10 000) $m^2 s^{-2}$ or larger from $z \sim 120$–180 km at 9 h east (west) of $x \sim 100$ km. SGWs contribute very little to eastward MFs, as these motions comprise largely ducted responses east of SP at $z \sim 87$–105 km. SGWs propagating westward exhibit significant negative MFs having magnitudes of ~1000–3000 $m^2 s^{-2}$ west of SP above $z \sim 130$ km at 9 h, but no significant MFs earlier or later.

MFs over NP above $z = 115$ km are delayed compared to those over SP due to later and weaker MW breaking at more limited altitudes of $z \sim 52$–70 km. They achieve maxima from $z \sim 120$–180 km having positive (negative) magnitudes of ~300–700 (500–1000) $m^2 s^{-2}$ from 8.5 h to late times. Relative to SP, those over and east of NP reveal significantly greater variability in amplitude and sign at $z > 100$ km and $x > 0$. This is because SGWs arising from the extended downstream breaking east of NP make significant contributions to MFs at upstream and downstream locations.

Streamwise-averaged MFs in $y$–$z$ planes at $x = 0$, 50, and 100 km from 8 to 10 h, and in $x$–$y$ planes at $z = 50$ and 70 km from 8 to 10 h and $z = 100$ km at 9 and 10 h are shown at right in Figs. 4 and 5. These confirm the largely negative MW MFs over, between, and south and north of SP and NP, extending downstream and upstream with increasing time. Specific features include the following:

1) significant spatial and temporal variability of $\langle u'w' \rangle$ due to MW breaking that reduces amplitudes and requires several $T_b$ to recover,
2) stronger mean $\langle u'w' \rangle$ correlated with the regions of most persistent MW breaking,
3) delayed and persistent weaker responses at lower altitudes to later times over NP than SP,
4) spatial variability along $y$, extending downstream and upstream at 70 km and largely upstream at 100 km, in time, and bowing westward over and between SP and NP, and
5) correlations of stronger local upstream bowing over SP and NP increasing with altitude.

MFs above ~100 km in Fig. 4 reveal that highly variable SGWs and AWs seen in the $x$–$z$ planes over SP and NP are not isolated responses to those peaks, but that major transports of momentum into, and forcing of the thermosphere by, these motions appear to arise preferentially in regions of strongest MW breaking in the stratosphere, especially over and south of SP. In particular, responses at $x = 50$ and 100 km north of SP at 10 h suggest SGWs having positive MFs, implying upward propagation toward the NE, superposed with larger-scale AWs propagating west of north (see the AWs and SGWs in these regions in Figs. 2 and 3). These responses are consistent with those seen in the $x$–$y$ cross sections at $z = 180$ km in Fig. 7.

Both the $y$–$z$ and $x$–$y$ cross sections in Figs. 4 and 5 reveal that the southern Andes MW responses are stronger and extend farther south than north of the domain center, reflecting the extended and narrower terrain to the S in Fig. 1. This variability is illustrated at top in Fig. 8 with probability distribution functions (PDFs) of MW $\log_{10}|\langle u'w' \rangle|$ for negative magnitudes from ~30 to 1200 $m^2 s^{-2}$ in the model domain extending from $x = 0$–100 km and $z = 40$–87 km for $y$ at NP, 0, SP, and $y = -250$ km and 8, 9, and 10 h. The PDFs reveal significant diversity that can be summarized as follows:

1) initial |MF| responses at 8 h are ~300–600 $m^2 s^{-2}$ east of SP, with less widespread (by ~2 times), but comparable, maxima east of NP and at $y = -250$ km, but much weaker at $y = 0$,
2) magnitudes >1000 $m^2 s^{-2}$ extend over larger and smaller regions at 9 h at $y = -250$ km and SP, respectively, with decreasing magnitudes and extents east of NP and at $y = 0$, and
3) peak |MF| magnitudes remain east of the southern Andes at $y = -250$ km and SP, and are larger and more frequent east of NP than at $y = 0$, but decrease at all locations by 10 h.

Zonal MF cospectra at an altitude of $z \sim 50$ km, averaged over 100 km in $y$ centered on each peak and from 7.5 to 9 h are shown in the lower panels of Fig. 8. These confirm that the MW MFs were significantly larger over SP than NP, with a peak magnitude twice as high, a broader range of $\lambda_x$ contributing significantly, and an integrated MF ~3 times larger. SP MFs spanned a range of scales from $\lambda_x \sim 48$–75 km with the peak at $\lambda_x \sim 60$ km that is consistent with that seen in Fig. 2 at 8 and 8.5 h. By comparison, NP led to weaker magnitudes at more discrete scales from $\lambda_x \sim 45$–80 km, with a peak response at $\lambda_x \sim 50$ km that is consistent with the NP fields in Fig. 3 at these times.

## 4. Mean-flow forcing, evolution, and correlations with zonal mean wind shears

### a. *Mean-flow evolution*

Complex MW generation and dissipation processes described above, especially modulations of $u$ and distortions of MW phases along the southern Andes, imply significant spatial and temporal variability in the evolving mean responses. The dominant contribution occurs via the vertical flux of horizontal momentum given by $dU/dt = -(1/\rho)d(\rho\langle u'w' \rangle)/dz < 0$. Thus, $dU/dt$ maxima largely occur above the MF maxima seen in Figs. 2–4 and are expected to yield the following:

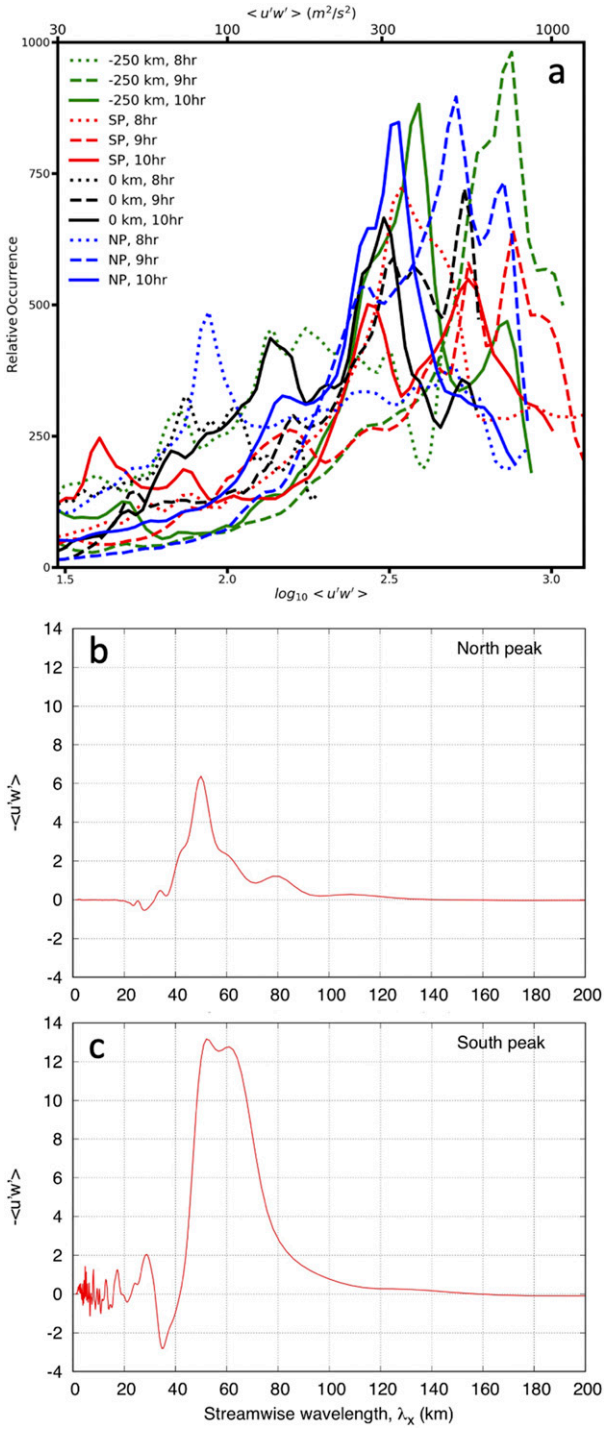


FIG. 8. (a) PDFs of $\langle u'w' \rangle$ in the model domain extending from $x$ = 0 to 100 km and $z$ = 40 to 87 km for $y$ at NP, 0, SP and 8, 9, and 10 h (see legend at upper left). (b),(c) $\langle u'w' \rangle(\lambda_x)$ at $z$ = 50 km in the lee of NP and SP averaged from 7.5 to 9 h. Note the very different $\lambda_x$ of the peaks responses and the very different integrated MFs due to the different SP and NP terrain.

1) increasing negative $\Delta U$ following volumes in which MW breaking is sustained,
2) variable $dU(x, y, z, t)/dt$ and $\Delta U$ that cause induced $U$ over, under, and around these regions,
3) induced deviations from the initial $U_0(z)$ extending further downstream with time despite peak forcing remaining in the near lee of the southern Andes throughout the MW responses, and
4) radiation of large-scale SGWs due to temporal variability.

Importantly, however, the full response is via the full 3D pseudomomentum flux and divergence over the entire domain, which will be explored more fully below.

The cumulative influences of MW and SGW momentum transport up to 10 h below the MW critical level at $z$ = 115 km are examined here. For these purposes, $x$–$z$ cross sections of the cumulative changes in $U$, denoted $\Delta U$, over NP, at $y$ = 0, and over SP are shown for $x$ from −200 to 600 km and $z$ = 30–115 km at 8, 9, and10 h in Fig. 9. A broader perspective along the southern Andes is provided with $y$–$z$ cross sections of $\Delta U$ for $z$=30–115 km spanning the region of strongest MW breaking from $x$ = 0–600 km shown at 9 and 10 h in Fig. 10. Profiles at 0, 8, 9, and 10 h are also shown at $x$ = −200, 0, 200, and 400 km and at $y$ = −400 km, SP, 0, NP, and 400 km in Fig. 11 to illustrate the evolutions of compensating (due to continuity) mean motions more quantitatively.

Initial $\Delta U$ fields at 8 h exhibit maxima of ∼−80 and −100 m s$^{-1}$ at $z \sim$ 75 and 65 km and $x \sim$ 50 and 80 km east of NP and SP, respectively (see upper panels at the top and bottom in Fig. 9). Clear differences in the responses over NP and SP arise by 9 h. Each field also has weaker $\Delta U$ extending downstream ∼100–200 km at higher altitudes at this time. The response at $y$ = 0 is only beginning to exhibit instability dynamics at ∼80 and above ∼100 km at 8 h, but already exhibits an accelerated $U$ at $z \sim$ 75 km and $x \sim$ 100–200 km accompanying the decelerations over NP and SP. All three $x$–$z$ cross sections exhibit enhanced eastward $U$ above the minimum at 87 km and extending to ∼110 km over NP and SP, but only to ∼100 km E at $y$ = 0 due to the higher initial MW breaking at this location and time. $\Delta U$ again becomes negative approaching the MW critical level at $z$ = 115 km from upstream to $x \sim$ 200 km at all three $y$ positions at 8 h. Importantly, significant variability along $x$ is seen at all three $y$ at MW $\lambda_x \sim$ 40 km and larger scales at this time.

The $\Delta U$ responses intensify strongly by 9 h, but differ among them in significant ways over and east of the southern Andes. All three exhibit the largest negative $\Delta U$ at $z \sim$ 50–70 km and $x \sim$ 0–120 km. But these are lower, deeper, and extend with larger magnitudes further east of SP, where a thin layer of $\Delta U \sim -100$ m s$^{-1}$ extends beyond $x \sim$ 300 km. $\Delta U$ east of NP and at $y$ = 0 are weaker and more uniform in altitude above $z \sim$ 60 km to $x \sim$ 300 km, compared to east of SP. Downstream responses at 9 h at all $y$ are more uniform by $x$ = 600 km and include

1) $\Delta U \sim -30$ to −50m s$^{-1}$ at $z \sim$ 65–87 km,
2) $\Delta U \sim$ 15 to 30 m s$^{-1}$ at $z \sim$ 87–105 km, and
3) variable $\Delta U$ along $x$ at $x >$ 150 km due to larger-scale SGWs at these altitudes.

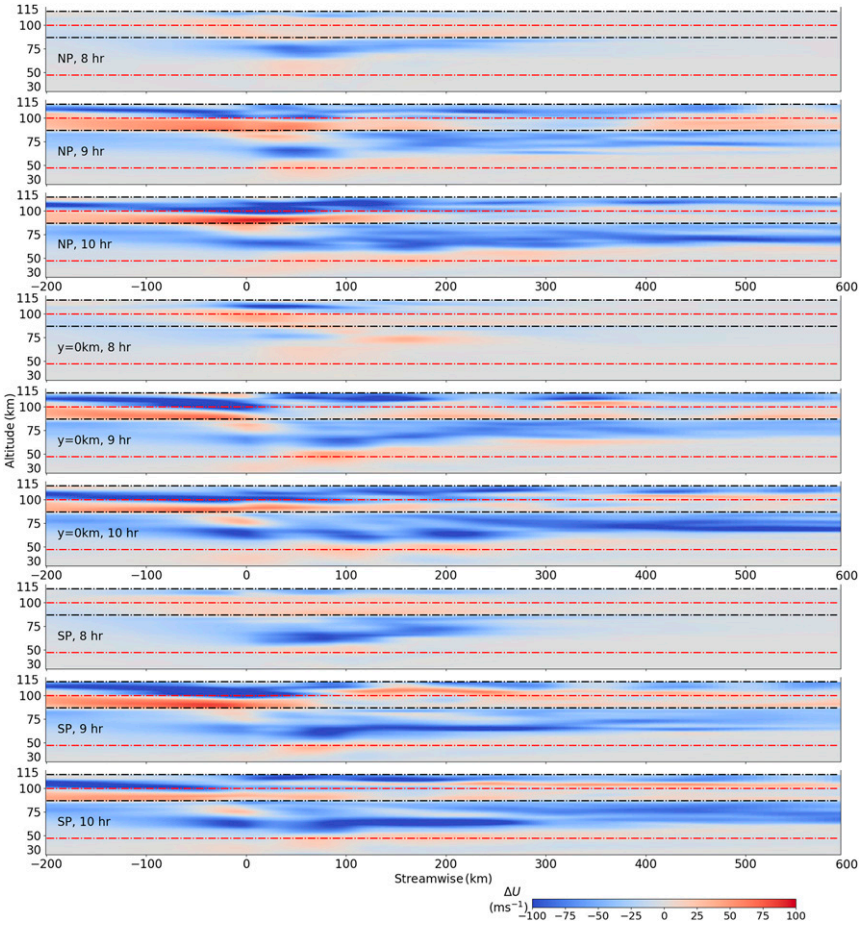


FIG. 9. (top to bottom sets) $\Delta U(x, z)$ over NP, at $y = 0$, and over SP from $z = 30$ to 115 km and $x$ from −200 to 600 km at (top to bottom in each set) 8, 9, and 10 h. Black (red) dashed lines denote eastward (westward) initial $U_0$ maxima in each panel. Note the increasing extensions of large $\Delta U < 0$ to large $x$ and correlations of $\Delta U$ and $dU/dz$ with increasing time.

Also seen to arise by 9 h at the three $y$ locations approaching $x = -200$ km are

4) increasing decelerations above ~50 km to $\Delta U \sim -60$ to $-70$ m s$^{-1}$ at $z \sim 85$ km,
5) positive $\Delta U \sim 50$ to 70 m s$^{-1}$ from $z \sim 87$ to above 100 km, and
6) strong, shallow $\Delta U \sim -70$ to $-90$m s$^{-1}$ at $z \sim 110$ km.

As at 8 h, variability in $\Delta U$ remains significant in regions of strong MW and SGW dynamics and breaking downstream and upstream of the southern Andes at 9 h, but occurs at larger scales at greater downstream distances. Notably, upstream variations of $\Delta U$ in $z$ are much larger than those downstream at 9 h, and they remain larger above 87 km at later times.

These trends change systematically thereafter, case becoming more structured in $z$, with negative and positive $\Delta U$ becoming more negative from 9 to 10 h. Importantly, large differences between the three $\Delta U$ $x$–$z$ cross sections arise, especially at downstream locations due to variable $\Delta U$ driven by variable $dU/dt$ and subsequent influences of induced $\nabla\rho$ accompanying $\Delta U$. These yield baroclinic generation of horizontal vorticity, $d\zeta_{x,y}\, dt^{-1} = (\nabla\rho x \nabla p)_{x,y}$, that act as sources of larger-scale SGWs where $(\nabla\rho)_{x,y}$ are nonzero. Time scales for disappearance of smaller-scale horizontal variability in $\Delta U$ fields advecting downstream are likely indicators of the $\omega_i$ of SGWs arising from this forcing. Disappearance of ~100-km scales in Fig. 8 at 9 and 10 h advecting ~200 km at $U \sim 80$ m s$^{-1}$ (at $z \sim 65$ km) implies an SGW time scale $T_{\mathrm{SGW}} \sim$ (200 km)/(80 m s$^{-1}$) ~ 40 min. This is roughly consistent with the period of an SGW $\lambda_z \sim 15$ km assumed to be ~ twice the depth of $\Delta U$ features seen in Fig. 8, $\lambda_x \sim$ 100 km, and $T_b \sim 314$s given by $(\lambda_x/\lambda_z)T_b \sim 35$ min.

Another perspective on the induced mean flow is provided with $\Delta U(y, z)$ cross sections from $x = 0$–600 km in Fig. 10. As suggested by Fig. 9 at $x = 0$ at 9 and 10 h, $\Delta U(y, z)$ at $x = 0$ at both times in Fig. 9 reveal significant consistency in the mean response along the southern Andes over the higher terrain as the response intensifies and extends along the southern Andes. This is especially true at $z \sim$ 60–80 km in the mesosphere, where $\Delta U$ are induced by MW breaking and momentum

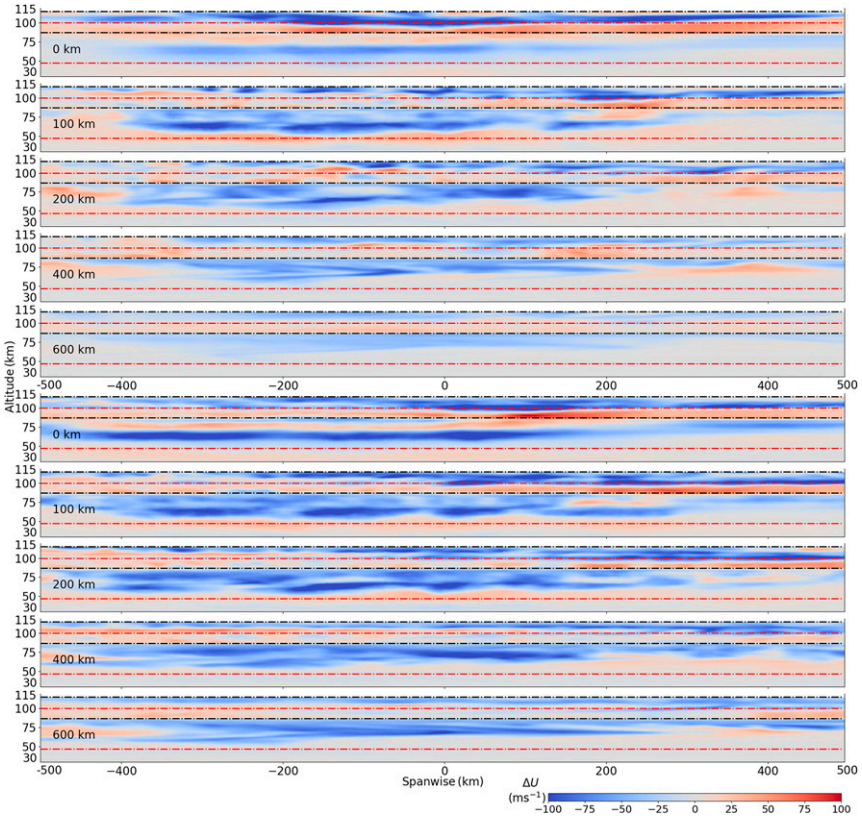


FIG. 10. $\Delta U(y, z)$ at (top) 9 and (bottom) 10 h from $z = 30$ to 115 km and (top to bottom in each set) $x = 0$ to 600 km. Note the increasing extensions of large $\Delta U < 0$ to large $|y|$ and correlations of $\Delta U$ and $dU/dz$ with increasing time, with dashed lines as in Fig. 9.

deposition beginning at $x \sim 30$ km that does not progress upstream to $x = 0$ until larger-scale MW components having smaller $\omega_i$ emerge and extend upstream at lower altitudes. Responses at $x = 0$ are more variable approaching the critical level at $z = 115$ km due to different terrain influences on the MW dynamics at $x > 0$ that contribute the responses at $x = 0$. The $\Delta U$ fields at larger $x$ at both times exhibit spatial variability along $y$ that is consistent with the reduction in smaller $\Delta U$ scales seen at comparable $x$ in Fig. 8 due to lee SGW generation noted above. $y$–$z$ cross sections at larger $x$ also reveal substantial influences of MW- and SGW-induced $\Delta U$ on the mean flow extending far downstream, from MW breaking altitudes into the MLT, and to large distances north and south of the major southern Andes orography.

Turning to Fig. 11, we note that $U(z)$ in the $x$–$z$ plane over SP are generally representative of those extending ~200–300 km further south as well. As described above, influences of local $dU/dt$, baroclinic generation of SGWs, and large-scale nondivergence have direct and indirect influences extending upstream, downstream, and to other altitudes and latitudes. Considering the $U(z)$ profiles at 8 h, we see the most significant decelerations to occur over and downstream of SP and NP below the $U_0$ minimum at ~87 km, with lower (higher) $\Delta U < 0$ at $x = 0$ and 200 km over and east of SP (NP), and larger accumulated $\Delta U$ over and east of SP due to the earlier and lower onset of MW breaking. Smaller $\Delta U < 0$ also accompany MW breaking below the critical level at $z = 115$ km, compensating weak $\Delta U > 0$ are seen at $z \sim 87$–100 km over and east of SP and NP and more strongly at $x = y = 0$, and all profiles at $x = -200$ and 400 km exhibit largely weak $\Delta U < 0$ at 8 h.

The $U(z)$ profiles shown in Fig. 11 (and elsewhere) become much more structured in altitude by 9 and 10 h (also see Figs. 9 and 10) due to coupling among $\Delta U$, MW $\lambda_z$, vertical propagation, and breaking amplitudes; see especially the amplifying oscillations in $U(z)$ over and east of SP and NP, and also at $y = 0$ and $x = 0$ and 100 km. The net effects at upstream locations from SP to NP are $\Delta U < 0$ from $z \sim 40$–85 and ~100–110 km and $\Delta U > 0$ from $z \sim 85$–100 km (and similar responses at larger and smaller $y$). Those at downstream locations include weaker $\Delta U > 0$ at $z \sim 50$ and 100 km and enhanced $\Delta U > 0$ at these altitudes at much larger $|y|$ (see Fig. 10). The overall MW response is thus major drag and $\Delta U < 0$ at breaking altitudes extending large distances along the southern Andes and downstream, with enhanced zonal flows below, above, between, and around these regions driven by continuity.

### b. *Correlations of $\Delta U$ and zonal wind shears*

Red lines in Figs. 9 and 10 indicate initial $U$ maxima at $z \sim 45$ and 100 km, and black lines indicate a $U \sim 10$ m s$^{-1}$ minimum at $z \sim 87$ km and a MW critical level ($U = 0$) at 115 km. $U$

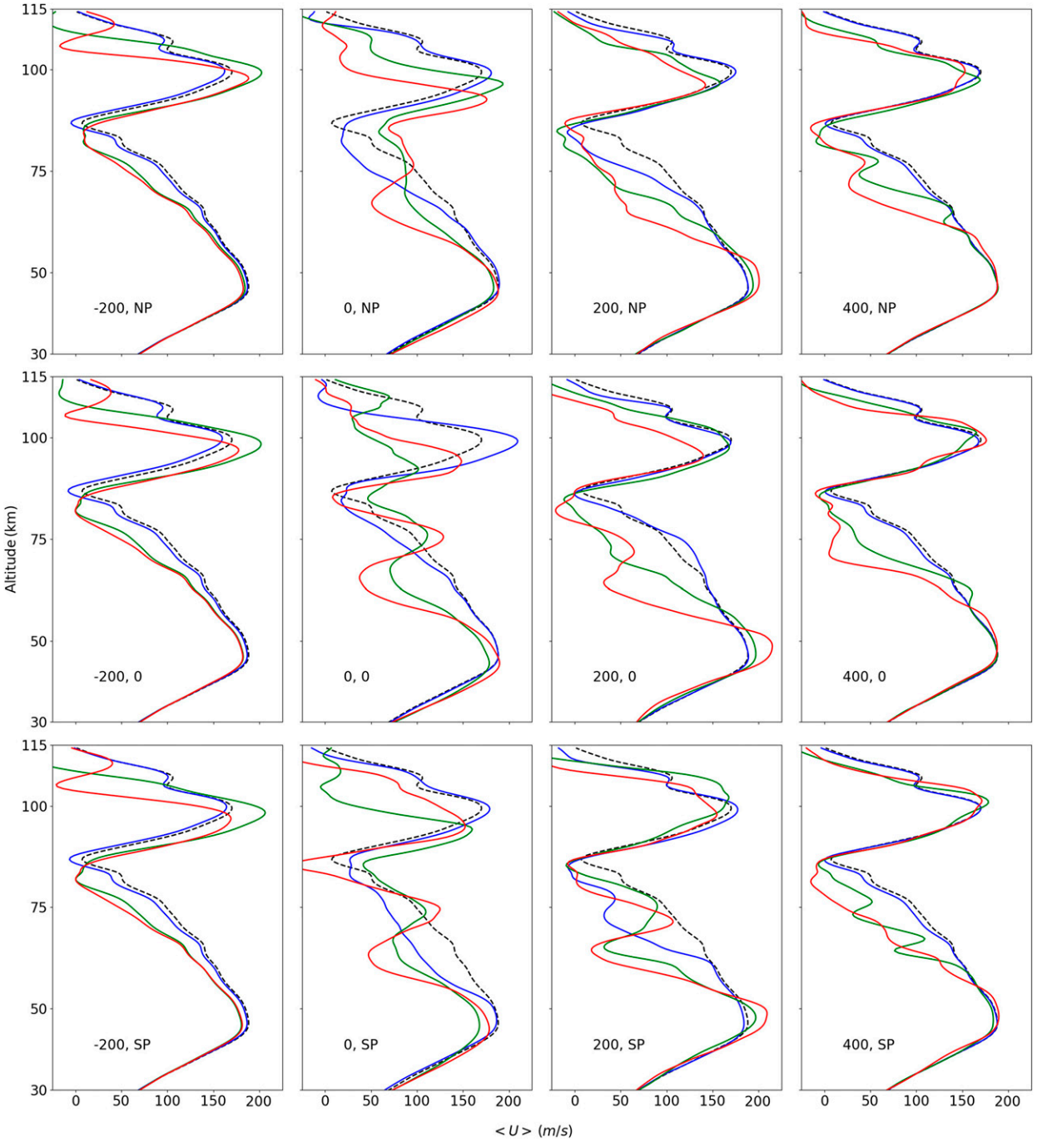


FIG. 11. Evolving $U(z)$ over (top to bottom) NP, at $y = 0$, and over SP at (left to right) $x = -200, 0, 200$, and 400 km at 0 (black dashed), 8, 9, and 10 h (blue, green, and red, respectively). Note the major departures from $U_0$ and the significant and increasing variability over and in the lee of the southern Andes arising from sustained MW breaking and pseudomomentum deposition.

differences between red and black lines are >150 m s$^{-1}$ in each case (Fig. 1), and the implied $dU/dz$ have dramatic influences on MW and SGW evolutions, and their effects on the evolving $U(x, y, z, t)$. Between $z \sim 50$–60 km, where MW breaking begins, and the $U$ minimum at $z \sim 87$ km, MWs refract to smaller $\lambda_z \sim 2\pi U/N$ and their amplitudes are constrained by $|u'| \sim |c_i|$ $\sim |U_h|$ for phase speeds $c \sim 0$. This results in large negative $dU/dt$ and $\Delta U$ that are correlated with $dU/dz$ at these altitudes and extend upstream and downstream with time, as discussed above (Figs. 9 and 10). The same dynamics arise at altitudes between the $U$ maximum at ~100 km and the critical level at ~115 km where MWs penetrating the $U \sim 10$ m s$^{-1}$ minimum

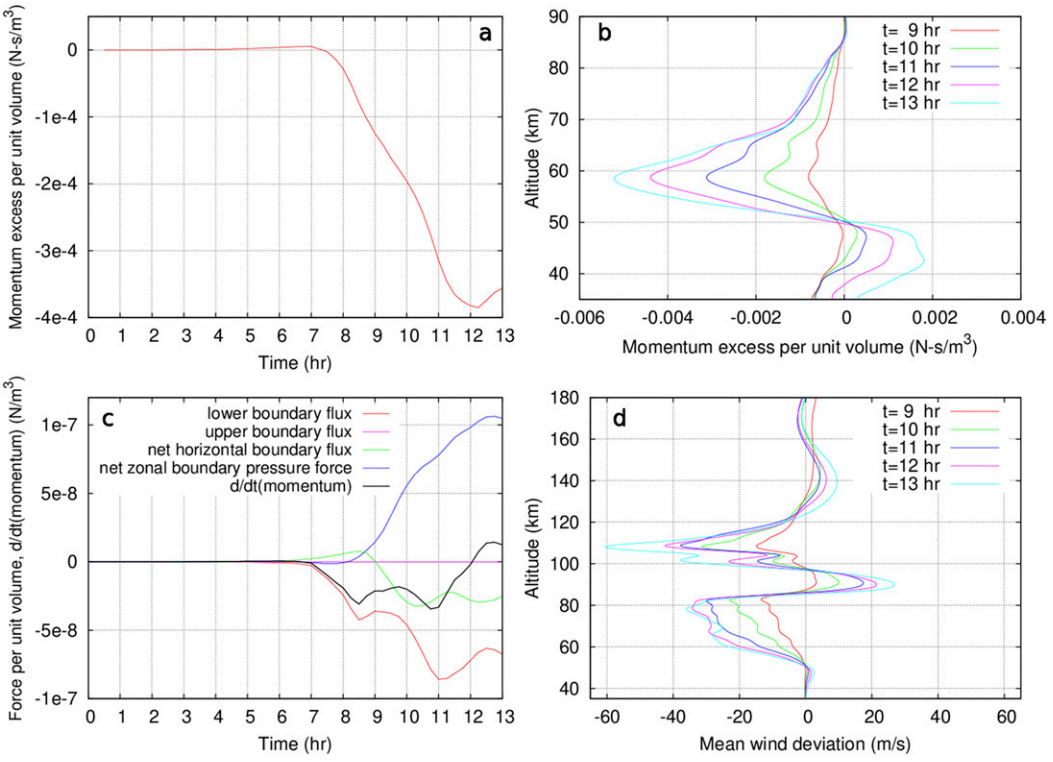


FIG. 12. (a) Domain-integrated momentum change at altitudes from 35 to 90 km, and (b),(c) vertical profiles and domain averages of the contributing dynamics [see legend in (c)]. (d) Zonal mean wind deviations from 35- to 180-km altitudes are shown from 9 to 13 h.

at $z \sim 87$ km have increasing $|u'|$ prior to the same $|u'| \sim |c_i| \sim |U_h|$ constraint above $z \sim 100$ km.

Between $z \sim 87$ and 100 km, in contrast, $dU/dz$ is large and positive, and MW $|u'|$ increases with altitude are not constrained by increasing $U$. SGWs generated by MW breaking below also readily propagate toward the east and west at these altitudes. However, SGWs propagating westward will have negative MFs and induced $\Delta U$, hence cannot account for the $\Delta U > 0$ seen over and west of the southern Andes at $z \sim 87$–100 km. Ducted SGWs at these altitudes with $c > 0$ at $x > 0$ can contribute $\Delta U > 0$ where they are dissipated, but account for only weak $\Delta U > 0$ further downstream. Thus, neither MWs nor SGWs account for the significant $\Delta U > 0$ west of the southern Andes at $z \sim 87$–100 km. Rather, this region of strong $\Delta U > 0$ must instead be driven by compensating enhanced eastward local mean flows over, under, and around the regions experiencing strong decelerations or westward mean-flow reversals constrained by $\nabla \cdot (\rho \mathbf{U}) = 0$. More direct evidence of this is seen in Fig. 10, which suggests offsetting positive and negative $\Delta U$.

### c. *Full domain momentum balance*

We now examine the integrated fluxes and forcing contributing to the changing zonal mean momentum at altitudes from 35 to 90 km (between the prescribed mean wind forcing below 35 km and the $U_0$ minimum at ~87 km). The domain-integrated momentum change and vertical profiles of the contributing dynamics are shown from 9 to 13 h in Figs. 12a and 12b. Temporal evolutions of the domain-averaged contributing fluxes, lateral pressure force, and rate of change of mean eastward momentum are shown in Fig. 12c. Figure 12d shows profiles of the zonal mean wind deviations at 35–180 km from 9 to 13 h.

Figure 12a reveals virtually no change above $z \sim 35$ km until ~7 h, at which time MW amplitudes and MFs first become significant. This delay is due to the slow ramp in MW forcing and the small vertical group velocities in the weaker $U_0(z, t)$ below 35 km. Thereafter, mean eastward momentum decreases strongly, with the most rapid decreases occurring at ~8–9 h and ~10.5–11.5 h. Referring to Figs. 3–5 of L20, we see that these times of more rapidly decreasing momentum correspond to the stronger MW and SGW activity above 35 km and the relative minima of the lower boundary flux seen in the red line in Fig. 12b. A weak increase occurs after ~12 h that we attribute to MW breaking below ~30 km seen in Fig. 7 of L20 beginning as the forcing approaches it maximum, which results in decreasing MW amplitudes and MFs from below (see Fig. 12b, red line).

Horizontally averaged momentum profiles shown in Fig. 12c demonstrate decreasing eastward momentum emerging prior to 9h that have a primary maximum at ~58 km and a weaker secondary maximum emerging at ~65 km at the same time but diminishing in its contribution at later times (also see Figs. 2 and 3). FWHM of the combined profiles are ~10–12 km at each time. The larger and smaller peaks correlate closely with the upper edges of the regions having the strongest MW breaking

and maximum MFs in the lee of SP and NP, respectively. Importantly, the observed profiles include the full pseudomomentum flux and divergence influences though the MF cross sections in L20 do not. The momentum profiles exhibit 1) increases to zero near 50 km, at which MW breaking begins in the stratosphere in the lee of SP and 2) increases to zero at ~85–90 km, as expected given critical level approach at ~87 km. Hence, these responses are consistent with mean forcing due to continuing MW MFs and divergence at these altitudes.

In contrast, domain-averaged momentum increased between 40 and 50 km, despite apparent conservative MW propagation at these altitudes. Below 40 km, a momentum deficit is seen at 9 h that may be a consequence of momentum deposition due to SGS suppression of earlier, unresolved MW breaking in weaker $U$. This deficit is replaced by a momentum excess thereafter, as above 40 km. The momentum increase at these altitudes is due largely to the net zonal pressure force (Fig. 12c, blue line). There is also a small net momentum flux across the lateral boundaries accompanying largely downstream (upstream) exiting of MWs at earlier (later) times (Fig. 12c, green line). Of these influences, the net pressure force at the upstream/downstream boundaries is much more significant and largely balances the momentum flux across the lower boundary. The net rate of change is thus fairly small and even becomes positive at the latest times. There is no significant momentum flux or viscous force at the top boundary at 90 km.

The evolving horizontally averaged mean wind deviations shown in Fig. 12d reveal increasing deviations with time and clear correlations of increasing (decreasing) $\Delta U(z, t)$ and positive (negative) $dU/dz$ because of the tendency for preferential MW and SGW breaking and momentum deposition for decreasing $|c_i|$ and $\lambda_z$, and conservative MW and SGW amplitude growth for increasing $|c_i|$ and $\lambda_z$.

## 5. Discussion

Our extension of the L20 study reveals that large MW amplitudes and $\lambda_z$, and small $\lambda_x$, result in large and variable momentum fluxes having major influences on atmospheric structure and variability extending from the stratosphere into the MLT and over large distances horizontally. These effects accompany large momentum flux divergence due to strong, large-scale instabilities driving MW breaking, and corresponding large and variable local body forcing via MW MF divergence. Though we do not assess 3D pseudomomentum fluxes and divergence, they are included implicitly in the flow evolution. These influences yield significant local mean-flow decelerations, additional SGW generation, and mean-flow responses extending over large regions.

CGCAM modeling results described above include the following:

1) results of previous, high-resolution, DNS modeling studies addressing the dominant dynamics due to MW and more general GW breaking are confirmed,
2) MF magnitudes are consistent with multiple, previous assessments of large, local GW MFs accompanying breaking in multiple observational studies,
3) they reveal where various assumptions regarding GW breaking that are widely employed are not justified, and
4) they provide new insights into MW, SGW, AW, and more general GW influences on their environments extending into the thermosphere.

GW overturning was suggested to lead to breaking, turbulence generation, and GW amplitude limits over 50 years ago, and our results confirm those assumptions and quantify their implications for MWs. More recent studies employed Ri- and ''Lindzen''-type constraints on GW amplitudes and MWs that remain in use in various mesoscale and global models (Garcia et al. 2007; Kruse and Smith 2015). However, results of this study confirm predictions of earlier idealized DNS and direct observations in the MLT exhibiting large GW amplitude decreases due to breaking and the implied time scales for amplitude and MF modulations (F02; F09a,b; F17; T19).

Additional insights provided by our southern Andes MW simulation include the following:

1) peak MW MFs in the MLT are highly localized due to small MW $\lambda_x$ and localized breaking,
2) peak MW MFs are ~300–1200 $m^2 s^{-2}$, thus comparable to the largest previous estimates,
3) virtually all MW MF in the lee of the Andes are associated with MW $\lambda_x \sim 100$ km or smaller,
4) localized body forcing and large-scale decelerations advect large distances downstream,
5) additional responses extend upstream, downstream, along $y$, and to other altitudes due to evolving mean flows over, under, and around those due to direct MW forcing,
6) $U(z)$ becomes more highly structured over and east of the southern Andes at later times, and
7) induced $U(z)$ become strongly correlated with $dU/dz$ from the lowest altitudes of MW breaking to the MW critical level at $z = 115$ km over a large region at later times.

These results have major implications for MW and general GW forcing of their environments, and for mesoscale and global modeling intended to describe these dynamics. The occurrence of the major vertical MFs accompanying small-scale MWs and other GWs implies local forcing and responses at spatial scales that cannot be resolved by global models. Results presented here and in previous assessments from the troposphere to the MLT suggest that the dominant MFs in the MLT accompany GWs having $\lambda_h \sim 100$ km or smaller. This is even the case over the New Zealand South Island, where the terrain extent exceeds 100 km, MLT MW $\lambda_x$ are as large as ~250 km, but the dominant MFs occur at $\lambda_x < 100$ km (B18; F18). The importance of smaller scales was also recognized in modeling of island responses by Vosper (2015), Vosper et al. (2016), and E16 that yielded similar implications for the importance, and required resolution, of smaller MW scales.

Instability dynamics demonstrated here, quantified in earlier idealized DNS (F09a,b), and seen in other ground-based and airborne observations cited above reveal that breaking GWs exhibit significant amplitude reductions that imply intermittency in local SGW forcing. Such intermittent, small-scale

forcing implies strong generation of SGWs, also having small $\lambda_h$, that likewise cannot be resolved by existing global models. The small scales and intermittency of these dynamics reveal the needs to 1) account for small-scale stochastic forcing by MWs and more general GWs in new parameterizations and 2) include parameterization of SGW sources in large-scale models, given that global model resolution able to describe these dynamics explicitly will likely not be available in the near future.

Our results reinforce the conclusions of a number of previous studies regarding implications of GW breaking at various altitudes for GW amplitude reductions, intermittency of sources and/or responses, and/or generation of SGWs (Satomura and Sato 1999; Lane and Sharman 2006; Chun and Kim 2008; Sato et al. 2009; Horinouchi et al. 2002). They also exhibit very similar responses to those of idealized CGCAM simulations addressing self-acceleration dynamics in less variable large-scale wind and temperature fields that more clearly reveal the SGW and AW responses to more localized sources and less structured thermospheres (D20; F20).

Pautet et al. (2021) employed OH airglow temperature imaging and meteor radar wind s at Rio Grande, Argentina (53.8°S, 67.7°W), to explore conditions that enabled MWs at altitudes of ~80–90 km during austral winter 2018. They showed MW occurrence at ~87 km to be strongly correlated with the eastward phase of the semidiurnal tide (SDT) when MW forcing and propagation at lower altitudes enabled their penetration into the MLT. Peak responses were observed at ~0400–0500 UT, consistent with the initial identification of MWs over the southern Andes from El Leoncito (31.8°S, 69.3°W) by Smith et al. (2009). MW MF estimates by Pautet et al. (2021) at 87 km were frequently as large as ~100–1000 $m^2$ $s^{-2}$, thus similar to magnitudes reported here below ~100 km in the lee of lower terrain at the extrema of our CGCAM MF fields in the central, high-resolution domain. More direct comparisons were not possible, however, because our simulation had $U \sim 0$ at 87 km and coarse resolution over Rio Grande. CGCAM would surely have yielded stronger MW responses and turning into the polar vortex at higher southern latitudes had the simulation included stronger mean winds at larger negative $y$, but that capability did not exist at the time of this simulation.

Ground-based Rayleigh lidar observations collocated with the imager and radar at Rio Grande provided additional MW MF assessments SE of the major southern Andes terrain in the stratosphere and up to 80 km in the mesosphere over the 2018 austral winter season. Aided by ECMWF IFS modeling, these analyses yielded peak $\rho_0\langle u_h' w'\rangle \approx 30$–$200$ mPa at 40–50 km (Kaifler et al. 2020), and decreasing to ~10 and 1 mPa at 60 and 70 km, respectively, that were significantly larger than the majority of satellite estimates at these altitudes. The estimates were related to MWs having large $\lambda_z$, sometimes for extended intervals. By comparison, CGCAM estimates at ~50–70 km in the lee of lower southern Andes terrain were ~100–250 $m^2$ $s^{-2}$, or as large as ~150 (10) mPa at 50 (70) km, thus comparable to, or somewhat larger than, the estimates by Kaifler et al. (2020). These comparisons are encouraging, but as above not for the same environments or terrain.

We also compare our simulated MW MFs in the stratosphere with previous stratospheric mean "absolute" GW MF estimates obtained using HIRDLS and SABER satellite measurements and mean GW MF estimates by various global models for latitudes of ~45°–50°S during austral winter 2006 (Geller et al. 2013). The satellite mean estimates were up to ~0.5–2 (~0.15–0.75) mPa at ~45°–50°S at 40 (50) km, respectively, whereas the model longitude means were ~4–10 times larger. The model estimates over the southern Andes were up to another ~10 times larger because the satellite measurements largely failed to capture the strong southern Andes responses, though more recent AIRS analyses yielded much larger MW MF estimates (Wright et al. 2017). In comparison, peak MW MFs in the lee of SP and NP at 50 km in our simulation were seen to be as large as ~1000 $m^2$ $s^{-2}$, or approximately ~500 mPa weighted by mean density, in localized regions extending ~50–100 km in $x$, and perhaps ~10 times smaller averaged over an extended region, with larger means at lower altitudes. Our CGCAM estimates are thus ~10–100 times larger than the mean "absolute" MFs measured by satellite and up to ~10 times those estimated by global the models in this region.

Finally, our results provide new insights into responses to flow decelerations accompanying local MW breaking and pseudomomentum deposition addressed using 2D simulations by Durran (1995). Specifically, our 3D simulation reveals emergence of complex and evolving responses to multiple MW and SGW breaking events resolving the breaking dynamics from ~20 to 120 km. Primary responses due to MW pseudomomentum deposition in regions of MW breaking include local 3D decelerations causing the local flow to divert under, over, and around these regions. These arise preferentially, and yield systematic and sustained $U(z)$ decreases, where $dU/dz < 0$ causes decreasing MW $c_i$, $\lambda_z$, and enhanced breaking. Upstream and downstream pressure perturbations also arise that contribute net volume-averaged $U(z)$ accelerations below the altitudes of primary MW breaking, confirming the results of Durran (1995) for resolved, 3D MW breaking. The extended downstream decelerations are also consistent with those noted in the ECMWF IFS analyses reported by Kaifler et al. (2020).

## 6. Conclusions

A number of results of our modeling described above were, or could have been, anticipated based on high-resolution observations and/or modeling of specific events at lower and higher altitudes. Examples include intermittency of GW breaking, instability character and scales, pseudomomentum deposition, local body forcing, and their implications for mean-flow forcing and evolution, and SGW and AW generation. Given that the simulation described here links all of these elements, it provides an example of how these dynamics operate throughout the atmosphere in a self-consistent way, linking the MW forcing scales to the response scales in the stratosphere and MLT. What may not have been quantified fully, nor appreciated previously, are the small-scale implications for much larger-scale responses. These include the significant $U(z)$ decelerations and layering, and their extensions over >1000 km

in latitude (and hundreds of kilometers north and south of the major orography), >600 km downstream, and to altitudes below and above those experiencing direct MF divergence.

These results suggest that similar responses should be expected for other larger and smaller MW sources that lead to significant MFs and deposition in the MLT, and likely similar responses due to MW breaking in the lower and middle stratosphere. They also suggest significant benefits of direct comparisons of such simulations with detailed MLT observations and global models describing the same local dynamics via parameterization in the same environments. The local dynamics described here is surely also relevant to more general GWs arising from other sources and undergoing similar nonlinear dynamics and local mean-flow interactions.

Our assessment of the force balance for domain means at intermediate altitudes are generally consistent with those of Durran (1995) at lower altitudes, and suggest potential benefits of a more complete analysis addressing these responses as functions of altitude that will be reported later.

*Acknowledgments.* Research described here was performed under Air Force Office of Scientific Research, National Science Foundation, and National Aeronautics and Space Administration grants cited in the Grant Electronic Management System. We also thank the Department of Defense High Performance Computing Modernization Program for access to computational resources that enabled this modeling study. Movies of these dynamics, figures, and data needed to replicate the figures herein are included as online supplementary files.

## REFERENCES

Alexander, M. J., and A. W. Grimsdell, 2013: Seasonal cycle of orographic gravity wave occurrence above small islands in the Southern Hemisphere: Implications for effects on the general circulation. *J. Geophys. Res. Atmos.*, **118**, 11 589–11 599, https://doi.org/10.1002/2013JD020526.

Bacmeister, J. T., 1993: Mountain wave drag in the stratosphere and mesosphere inferred from observed winds and a simple mountain-wave parameterization scheme. *J. Atmos. Sci.*, **50**, 377–399, https://doi.org/10.1175/1520-0469(1993)050<0377:MWDITS>2.0.CO;2.

——, and M. R. Schoeberl, 1989: Breakdown of vertically propagating two-dimensional gravity waves forced by orography. *J. Atmos. Sci.*, **46**, 2109–2134, https://doi.org/10.1175/1520-0469(1989)046<2109:BOVPTD>2.0.CO;2.

Bossert, K., and Coauthors, 2015: Momentum flux estimates accompanying multiscale gravity waves over Mount Cook, New Zealand, on 13 July 2014 during the DEEPWAVE campaign. *J. Geophys. Res. Atmos.*, **120**, 9323–9337, https://doi.org/10.1002/2015JD023197.

——, and Coauthors, 2018: Momentum flux spectra of a mountain wave event over New Zealand. *J. Geophys. Res. Atmos.*, **123**, 9980–9991, https://doi.org/10.1029/2018JD028319.

Bougeault, P., and Coauthors, 2001: The MAP Special Observing Period. *Bull. Amer. Meteor. Soc.*, **82**, 433–462, https://doi.org/10.1175/1520-0477(2001)082<0433:TMSOP>2.3.CO;2.

Bramberger, M., and Coauthors, 2017: Does strong tropospheric forcing cause large-amplitude mesospheric gravity waves? A DEEPWAVE case study. *J. Geophys. Res. Atmos.*, **122**, 11 422–11 443, https://doi.org/10.1002/2017JD027371.

Chun, H.-Y., and Y.-H. Kim, 2008: Secondary waves generated by breaking of convective gravity waves in the mesosphere and their influence in the wave momentum flux. *J. Geophys. Res.*, **113**, D23107, https://doi.org/10.1029/2008JD009792.

Dong, W., D. C. Fritts, T. S. Lund, S. A. Wieland, and S. Zhang, 2020: Self-acceleration and instability of gravity wave packets: 2. Two-dimensional packet propagation, instability dynamics, and transient flow responses. *J. Geophys. Res. Atmos.*, **125**, e2019JD030691, https://doi.org/10.1029/2019JD030691.

Doyle, J. D., M. Shapiro, Q. Jiang, and D. Bartels, 2005: Large-amplitude mountain wave breaking over Greenland. *J. Atmos. Sci.*, **62**, 3106–3126, https://doi.org/10.1175/JAS3528.1.

Durran, D. R., 1990: Mountain waves and downslope winds. *Atmospheric Processes over Complex Terrain*, *Meteor. Monogr.*, No. 23, Amer. Meteor. Soc., 59–83.

——, 1995: Do breaking mountain waves decelerate the local mean flow? *J. Atmos. Sci.*, **52**, 4010–4032, https://doi.org/10.1175/1520-0469(1995)052<4010:DBMWDT>2.0.CO;2.

——, and J. B. Klemp, 1987: Another look at downslope winds. Part II: Nonlinear amplification beneath wave-overturning layers. *J. Atmos. Sci.*, **44**, 3402–3412, https://doi.org/10.1175/1520-0469(1987)044<3402:ALADWP>2.0.CO;2.

Eckermann, S. D., and P. Preusse, 1999: Global measurements of stratospheric mountain waves from space. *Science*, **286**, 1534–1537, https://doi.org/10.1126/science.286.5444.1534.

——, and Coauthors, 2016: Dynamics of orographic gravity waves observed in the mesosphere over the Auckland islands during the Deep Propagating Gravity Wave Experiment (DEEPWAVE). *J. Atmos. Sci.*, **73**, 3855–3876, https://doi.org/10.1175/JAS-D-16-0059.1.

Fritts, D. C., and G. D. Nastrom, 1992: Sources of mesoscale variability of gravity waves. Part II: Frontal, convective, and jet stream excitation. *J. Atmos. Sci.*, **49**, 111–127, https://doi.org/10.1175/1520-0469(1992)049<0111:SOMVOG>2.0.CO;2.

——, L. Wang, J. Werne, T. Lund, and K. Wan, 2009a: Gravity wave instability dynamics at high Reynolds numbers. Part I: Wave field evolution at large amplitudes and high frequencies. *J. Atmos. Sci.*, **66**, 1126–1148, https://doi.org/10.1175/2008JAS2726.1.

——, ——, ——, ——, and ——, 2009b: Gravity wave instability dynamics at high Reynolds numbers. Part II: Turbulence evolution, structure, and anisotropy. *J. Atmos. Sci.*, **66**, 1149–1171, https://doi.org/10.1175/2008JAS2727.1.

——, and Coauthors, 2016: The Deep Propagating Gravity Wave Experiment (DEEPWAVE): An airborne and ground-based exploration of gravity wave propagation and effects from their sources throughout the lower and middle atmosphere. *Bull. Amer. Meteor. Soc.*, **97**, 425–453, https://doi.org/10.1175/BAMS-D-14-00269.1.

——, and Coauthors, 2017: High-resolution observations and modeling of turbulence sources, structures, and intensities in the upper mesosphere. *J. Atmos. Solar-Terr. Phys.*, **162**, 57–78, https://doi.org/10.1016/j.jastp.2016.11.006.

——, and Coauthors, 2018: Large-amplitude mountain waves in the mesosphere accompanying weak cross-mountain flow during DEEPWAVE research flight RF22. *J. Geophys. Res. Atmos.*, **123**, 9992–10 022, https://doi.org/10.1029/2017JD028250.

——, M. J. Taylor, P.-D. Pautet, N. R. Criddle, B. Kaifler, L. Wang, S. D. Eckermann, and B. Liley, 2019: Large-amplitude mountain waves in the mesosphere observed on 21 June 2014 during DEEPWAVE: 2. Nonlinear dynamics, wave breaking, and instabilities. *J. Geophys. Res. Atmos.*, **124**, 10 006–10 032, https://doi.org/10.1029/2019JD030899.

——, W. Dong, T. S. Lund, S. A. Wieland, and B. Laughman 2020: Self-acceleration and instability of gravity wave packets: 3. Three-dimensional packet propagation, secondary gravity waves, momentum deposition, and transient mean forcing in tidal winds. *J. Geophys. Res. Atmos.*, **125**, e2019JD030691, https://doi.org/10.1029/2019JD030691.

Garcia, R. R., D. R. Marsh, D. E. Kinnison, B. A. Boville, and F. Sassi, 2007: Simulation of secular trends in the middle atmosphere, 1950–2003. *J. Geophys. Res.*, **112**, D09301, https://doi.org/10.1029/2006JD007485.

Geller, M. A., and Coauthors, 2013: A comparison between gravity wave momentum fluxes in observations and climate models. *J. Climate*, **26**, 6383–6405, https://doi.org/10.1175/JCLI-D-12-00545.1.

Germano, M., U. Piomelli, P. Moin, and W. H. Cabot, 1991: A dynamic subgrid-scale eddy viscosity model. *Phys. Fluids*, **3A**, 1760–1765, https://doi.org/10.1063/1.857955.

Grubišić, V., and J. M. Lewis, 2004: Sierra Wave Project revisited: 50 years later. *Bull. Amer. Meteor. Soc.*, **85**, 1127–1142, https://doi.org/10.1175/BAMS-85-8-1127.

——, and Coauthors, 2008: The Terrain-Induced Rotor Experiment. *Bull. Amer. Meteor. Soc.*, **89**, 1513–1534, https://doi.org/10.1175/2008BAMS2487.1.

Hecht, J. H., and Coauthors, 2018: Observations of the breakdown of mountain waves over the Andes Lidar Observatory at Cerro Pachon on 8/9 July 2012. *J. Geophys. Res. Atmos.*, **123**, 276–299, https://doi.org/10.1002/2017JD027303.

Hendricks, E. A., and D. James, S. D. Eckermann, Q. Jiang, and P. A. Reinecke, 2014: What is the source of the stratospheric gravity wave belt in austral winter? *J. Atmos. Sci.*, **71**, 1583–1592, https://doi.org/10.1175/JAS-D-13-0332.1.

Hoffmann, L., X. Xue, and M. J. Alexander, 2013: A global view of stratospheric gravity wave hotspots located with Atmospheric Infrared Sounder observations. *J. Geophys. Res. Atmos.*, **118**, 416–434, https://doi.org/10.1029/2012JD018658.

Horinouchi, T., T. Nakamura, and J.-I. Kosaka, 2002: Convectively generated mesoscale gravity waves simulated throughout the middle atmosphere. *Geophys. Res. Lett.*, **29**, 2007, https://doi.org/10.1029/2002GL016069.

Jasperson, W. H., G. D. Nastrom, and D. C. Fritts, 1990: Further study of terrains effects on the mesoscale spectrum of atmospheric motions. *J. Atmos. Sci.*, **47**, 979–987, https://doi.org/10.1175/1520-0469(1990)047<0979:FSOTEO>2.0.CO;2.

Jiang, J. H., D. L. Wu, and S. D. Eckermann, 2002: Upper Atmosphere Research Satellite (UARS) observation of mountain waves over the Andes. *J. Geophys. Res.*, **107**, 8273, https://doi.org/10.1029/2002JD002091.

Jiang, Q., and J. D. Doyle, 2004: Gravity wave breaking over the central Alps: Role of complex terrain. *J. Atmos. Sci.*, **61**, 2249–2266, https://doi.org/10.1175/1520-0469(2004)061<2249:GWBOTC>2.0.CO;2.

——, ——, and R. B. Smith, 2006: Interaction between trapped waves and boundary layers. *J. Atmos. Sci.*, **63**, 617–633, https://doi.org/10.1175/JAS3640.1.

Kaifler, B., N. Kaifler, B. Ehard, A. Dörnbrack, M. Rapp, and D. C. Fritts, 2015: Influences of source conditions on mountain wave penetration into the stratosphere and mesosphere. *Geophys. Res. Lett.*, **42**, 9488–9494, https://doi.org/10.1002/2015GL066465.

Kaifler, N., B. Kaifler, A. Dörnbrack, M. Rapp, J. L. Hormaechea, and A. de la Torre, 2020: Lidar observations of large-amplitude mountain waves in the stratosphere above Tierra del Fuego, Argentina. *Sci. Rep.*, **10**, 14529, https://doi.org/10.1038/s41598-020-71443-7.

Klemp, J. B., and D. K. Lilly, 1978: Numerical simulation of hydrostatic mountain waves. *J. Atmos. Sci.*, **35**, 78–107, https://doi.org/10.1175/1520-0469(1978)035<0078:NSOHMW>2.0.CO;2.

Kruse, C. G., and R. B. Smith, 2015: Gravity wave diagnostics and characteristics in mesoscale fields. *J. Atmos. Sci.*, **72**, 4372–4392, https://doi.org/10.1175/JAS-D-15-0079.1.

Lane, T. P., and R. D. Sharman, 2006: Gravity wave breaking, secondary wave generation, and mixing above deep convection in a three-dimensional cloud model. *Geophys. Res. Lett.*, **33**, L23813, https://doi.org/10.1029/2006GL027988.

Lilly, D. K., 1978: A severe downslope windstorm and aircraft turbulence induced by a mountain wave. *J. Atmos. Sci.*, **35**, 59–77, https://doi.org/10.1175/1520-0469(1978)035<0059:ASDWAA>2.0.CO;2.

——, and P. J. Kennedy, 1973: Observations of a stationary mountain wave and its associated momentum flux and energy dissipation. *J. Atmos. Sci.*, **30**, 1135–1152, https://doi.org/10.1175/1520-0469(1973)030<1135:OOASMW>2.0.CO;2.

Lund, T. S., D. C. Fritts, K. Wan, B. Laughman, and H.-L. Liu, 2020: Numerical simulation of mountain waves over the southern Andes. Part I: Mountain wave and secondary wave character, evolutions, and breaking. *J. Atmos. Sci.*, **77**, 4337–4356, https://doi.org/10.1175/JAS-D-19-0356.1.

Nastrom, G. D., and D. C. Fritts, 1992: Sources of mesoscale variability of gravity waves. Part I: Topographic excitation. *J. Atmos. Sci.*, **49**, 101–110, https://doi.org/10.1175/1520-0469(1992)049<0101:SOMVOG>2.0.CO;2.

——, ——, and K. S. Gage, 1987: An investigation of terrain effects on the mesoscale spectrum of atmospheric motions. *J. Atmos. Sci.*, **44**, 3087–3096, https://doi.org/10.1175/1520-0469(1987)044<3087:AIOTEO>2.0.CO;2.

Pautet, P.-D., and Coauthors, 2016: Large-amplitude mesospheric response to an orographic wave generated over the Southern Ocean Auckland Islands (50.7°S) during the DEEPWAVE project. *J. Geophys. Res. Atmos.*, **121**, 1431–1441, https://doi.org/10.1002/2015JD024336.

——, M. J. Taylor, D. C. Fritts, D. Janches, N. Kaifler, A. Dörnbrack, and J. L. Hormaechea, 2021: Mesospheric mountain wave activity in the lee of the southern Andes. *J. Geophys. Res. Atmos.*, **126**, e2020JD033268, https://doi.org/10.1029/2020JD033268.

Sato, K., S. Watanabe, Y. Kawatani, Y. Tomikawa, K. Miyazaki, and M. Takahashi, 2009: On the origins of mesospheric gravity waves. *Geophys. Res. Lett.*, **36**, L19801, https://doi.org/10.1029/2009GL039908.

Satomura, T., and K. Sato, 1999: Secondary generation of gravity waves associated with the breaking of mountain waves. *J. Atmos. Sci.*, **56**, 3847–3858, https://doi.org/10.1175/1520-0469(1999)056<3847:SGOGWA>2.0.CO;2.

Schoeberl, M. R., 1985: The penetration of mountain waves into the middle atmosphere. *J. Atmos. Sci.*, **42**, 2856–2864, https://doi.org/10.1175/1520-0469(1985)042<2856:TPOMWI>2.0.CO;2.

Smith, R. B., 1979: The influence of mountain waves on the atmosphere. *Advances in Geophysics*, Vol. 21, Academic Press, 87–230, https://doi.org/10.1016/S0065-2687(08)60262-9.

——, 2019: 100 years of progress on mountain meteorology research. *A Century of Progress in Atmospheric and Related Sciences: Celebrating the American Meteorological Society Centennial*, *Meteor. Monogr.*, No. 59, Amer. Meteor. Soc., https://doi.org/10.1175/AMSMONOGRAPHS-D-18-0022.1.

——, J. D. Doyle, Q. Jiang, and S. A. Smith, 2007: Alpine gravity waves: Lessons from MAP regarding mountain wave generation and breaking. *Quart. J. Roy. Meteor. Soc.*, **133**, 917–936, https://doi.org/10.1002/qj.103.

——, B. K. Woods, J. Jensen, W. A. Cooper, J. D. Doyle, Q. F. Jiang, and V. Grubisic, 2008: Mountain waves entering the stratosphere. *J. Atmos. Sci.*, **65**, 2543–2562, https://doi.org/10.1175/2007JAS2598.1.

Smith, S. M., J. Baumgardner, and M. Mendillo, 2009: Evidence of mesospheric gravity-waves generated by orographic forcing in the troposphere. *Geophys. Res. Lett.*, **36**, L08807, https://doi.org/10.1029/2008GL036936.

——, S. L. Vadas, W. J. Baggaley, G. Hernandez, and J. Baumgardner 2013: Gravity wave coupling between the mesosphere and thermosphere over New Zealand. *J. Geophys. Res. Space Phys.*, **118**, 2694–2707, https://doi.org/10.1002/jgra.50263.

Taylor, M. J., P.-D. Pautet, N. R. Criddle, D. C. Fritts, S. D. Eckermann, S. M. Smith, G. Hernandez, and M. McCarthy, 2019: Large-amplitude mountain waves in the mesosphere observed on 21 June 2014 during DEEPWAVE: 1. Wave development, scales, momentum fluxes, and environmental sensitivity. *J. Geophys. Res. Atmos.*, **124**, 10 364–10 384, https://doi.org/10.1029/2019JD030932.

Vosper, S. B., 2015: Mountain waves and wakes generated by South Georgia: Implications for drag parametrization. *Quart. J. Roy. Meteor. Soc.*, **141**, 2813–2827, https://doi.org/10.1002/qj.2566.

——, A. R. Brown, and S. Webster, 2016: Orographic drag on islands in the NWP mountain grey zone. *Quart. J. Roy. Meteor. Soc.*, **142**, 3128–3137, https://doi.org/10.1002/qj.2894.

Wright, C. J., N. P. Hindley, L. Hoffmann, M. J. Alexander, and N. J. Mitchell, 2017: Exploring gravity wave characteristics in 3-D using a novel S-transform technique: AIRS/Aqua measurements over the Southern Andes and Drake Passage. *Atmos. Chem. Phys.*, **17**, 8553–8575, https://doi.org/10.5194/acp-17-8553-2017.

Wu, D. L., and S. D. Eckermann, 2008: Global gravity wave variances from *Aura* MLS: Characteristics and interpretation. *J. Atmos. Sci.*, **65**, 3695–3718, https://doi.org/10.1175/2008JAS2489.1.